SEDIMENTOLOGY the journal of the International Association of Sedimentologists IAS

Sedimentology (2026) doi: 10.1111/sed.70077

Variations in downslope activity and bottom current dynamics in a land-detached submarine channel system since the Last Glacial Maximum

LOTTE VERWEIRDER*, AGGELIKI GEORGIOPOULOU†, KOBUS LANGEDOCK‡, FRED FOURIE‡, MARTIN WHITE§, SARA BENETTI¶, FABIO SACCHETTI**, WIETER BOONE‡ and DAVID VAN ROOIJ*

**Department of Geology, Ghent University, Krijgslaan 297, Ghent 9000, Belgium (E-mail: lotte.verweirder@ugent.be)*

†*Ternan Energy, Vantage Point, New England Road, Brighton BN1 4GW, UK*

‡*Flanders Marine Institute (VLIZ), Jacobsenstraat 1, Oostende 8400, Belgium*

§*School of Natural Sciences, University of Galway, University Road, Galway H91 TK33, Ireland*

¶*School of Geography and Environmental Sciences, Ulster University, Cromore Road, Coleraine BT52 1SA, UK*

***Marine Institute, Rinville, Oranmore H91 R673, Ireland*

Associate Editor – John Reijmer

ABSTRACT

The Gollum Channel System is a land-detached large-scale canyon-channel system situated offshore southwest Ireland on the Northeast Atlantic margin. The system has been considered inactive with downslope gravity flows since the last glacial period, but geophysical data in some of its branches do suggest Holocene activity. Here, the hypothesis of (in)activity under Holocene highstand conditions is tested. High-resolution side-scan sonar, photography and bathymetry data were collected using an autonomous underwater vehicle (AUV) in the upper slope (350 to 1000 m water depth) section of two channels in the system, Bilbo Channel and Frodo Channel. The AUV results are quantified and validated by current meter data from a mooring station in Bilbo Channel. Additionally, two sediment cores are used to build a record of channel floor processes since the Last Glacial Maximum and detect any temporal variability in channel activity. Turbidites in the sediment cores indicate that downslope sediment transport was happening well after deglaciation of the continental shelf, revealing that the channels were active under modern climatic and oceanographic conditions in the early Holocene. Crescentic bedforms in one of the channel head gullies suggest present-day activity, but their limited spatial extent indicates present-day downslope flows are minimal in frequency and volume. As a whole, the Gollum Channel System can be considered inactive today. Rather, tidally modulated bottom currents oriented along the channel axes are the main mechanism currently transporting and redistributing sediments, forming fields of mega-ripples and superimposed ripples. This dynamic channel floor environment has allowed the development of cold-water coral mini-mounds since the early Holocene. This study highlights that specific environmental conditions are necessary to allow frequent downslope activity in a land-detached canyon-channel system and these may vary even in systems draining the same shelf, and that inactivity may have important consequences for deep-sea habitats, by allowing or promoting their development.

Keywords Autonomous underwater vehicle, bottom currents, cold-water corals, Gollum Channel System, Porcupine Seabight, turbidity currents.

INTRODUCTION

Submarine canyon-channel systems are important geomorphological features that facilitate the downslope transport of sediments, nutrients and pollutants from shallow continental shelves to deep-water basins (Canals *et al.*, 2006; Puig *et al.*, 2014; Azpiroz-Zabala *et al.*, 2017; Kane & Clare, 2019; Maier *et al.*, 2019; Pierdomenico *et al.*, 2023; Baker *et al.*, 2024). Generally, land-detached systems are considered inactive in this regard, as they are too far away from terrestrial sources and input from, for example, fluvial systems or long-shore drift cells in the present-day highstand conditions (Covault & Graham, 2010). On the other hand, several processes are capable of resuspending shelf and slope sediments, transporting them across a shelf and feeding them into a (land-detached) canyon system (Puig *et al.*, 2014). These include earthquakes (e.g. Mountjoy *et al.*, 2014), anthropogenic activities (e.g. Daly *et al.*, 2018), storm wave loading (e.g. Puig *et al.*, 2004), slope failures (e.g. Hsu *et al.*, 2008), internal waves (e.g. Aslam *et al.*, 2018), dense shelf-water cascading (e.g. Canals *et al.*, 2006), hyperpycnal flows (e.g. Li *et al.*, 2018) and others. Recent monitoring has shown that in some land-detached systems, these processes enable a frequency and intensity of downslope activity similar to that in land-attached systems (Normandeau *et al.*, 2020; Heijnen *et al.*, 2022; Jaijel *et al.*, 2023). Thus, the idea of inactivity in land-detached systems during sea-level highstands is increasingly being challenged. This evokes the question whether frequent downslope activity should be expected in land-detached canyons globally or rather distinct environmental conditions allow or trigger regular activity in specific locations only. Considering c. 80% of all large-scale canyon-channel systems are land-detached (Harris *et al.*, 2014; Bernhardt & Schwanghart, 2021), and they are spread across all continental margins (Harris & Whiteway, 2011), the impact on our understanding of canyon system dynamics and canyon-associated deep-sea ecosystems, carbon cycle and marine geohazards, is potentially large.

To better understand the constraints on the inactivity hypothesis for land-detached submarine canyons, the Gollum Channel System (GCS) is an ideal study area. It is a large-scale land-detached system situated c. 100 km from the southwest coast of Ireland. The GCS is located on the same margin as the land-detached Whittard Canyon (Fig. 1), where frequent present-day downslope activity has been documented (Heijnen *et al.*, 2022). However, the two systems feed into different basins and may be linked to different sediment sources, which potentially affects the sediment dynamics within them. Whittard Canyon has been draining the Celtic Shelf and received input from the Irish Sea Ice Stream and Fleuve Manche paleoriver during the last glacial period (Bourillet *et al.*, 2006; Heijnen *et al.*, 2022). The GCS is thought to have drained the Celtic Shelf also, but this was never proven and the source of sediment supply to the GCS remains enigmatic (Tudhope & Scoffin, 1995; Wheeler *et al.*, 2003). Additionally, whereas present-day downslope activity has been documented in Whittard Canyon (Heijnen *et al.*, 2022), the GCS is considered inactive since the Last Glacial Maximum, when the British-Irish Ice Sheet extended onto the Celtic Sea Shelf (Wheeler *et al.*, 2003; Scourse *et al.*, 2021). Tudhope & Scoffin (1995) observed biological encrustation on dropstones and coral thickets during their submersible dives in one of the GCS tributaries, Bilbo Channel, from which they inferred no turbidity currents occurring for at least several decades before their dive. They also made visual observations of reversing bottom currents, for which they estimated maximum velocities of 0.5 m s^{-1}, and identified them as the main mechanism of present-day sediment transport (Tudhope & Scoffin, 1995). Current meter data from a 2005 mooring in Bilbo Channel confirmed the presence of tidally modulated bottom currents and did not record any downslope flows in the 185-day measurement period (Verweirder *et al.*, 2021). However, bathymetry data from the INFOMAR mapping programme of the Geological Survey Ireland and the Marine Institute (publicly available at https://www.infomar.ie/) reveal gullies in the channel heads of Bilbo and Frodo channels, the two northernmost channels of the system (Fig. 1B) (Geological Survey Ireland & Marine Institute, 2024), suggesting possible Holocene activity.

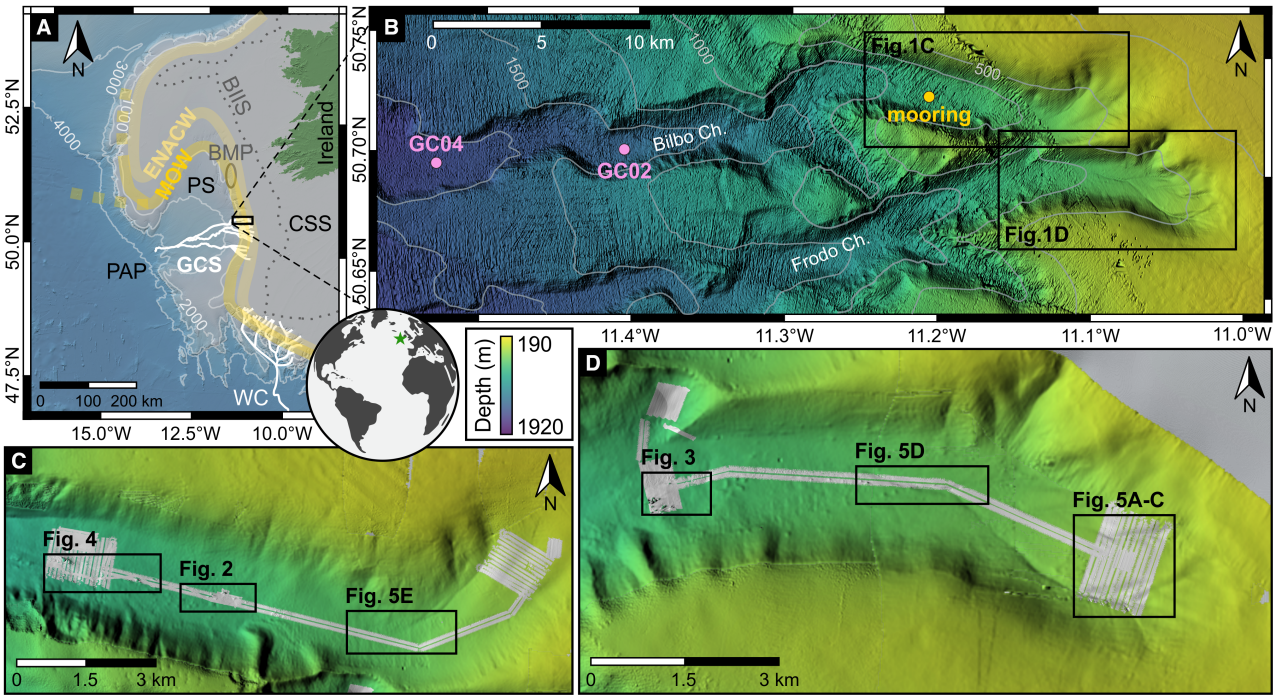

Fig. 1. (A) Topography map showing the Porcupine Seabight (PS) on the Northeast Atlantic margin. The bathymetry is the GEBCO_2023 Grid (GEBCO Compilation Group, 2023), with contour lines drawn every 1000 m. The Gollum Channel System (GCS) is indicated in white, stretching from the Celtic Sea Shelf (CSS) to the Porcupine Abyssal Plain (PAP). Whittard Canyon (WC) is also indicated in white. The grounding line of the British-Irish Ice Sheet (BIIS) at its maximum extent (c. 26 ka) is indicated as a grey dotted line and based on Clark *et al.* (2022a). The Belgica Mound Province (BMP) is indicated by a grey oval. The Eastern North Atlantic Central Water (ENACW) and Mediterranean Outflow Water (MOW) are carried northwards by the European Slope Current. (B) Bathymetry map showing the sections of Bilbo Channel and Frodo Channel that are the focus of this study. The location of the mooring from Verweirder *et al.* (2021) is indicated by the yellow dot. The locations of the two sediment cores described in this study (B2306-GC02 and B2306-GC04) are indicated by the pink dots. The bathymetry is the INFOMAR 25 m-resolution grid (Geological Survey Ireland & Marine Institute, 2024), with contour lines drawn every 250 m. (C) and (D) Close-up bathymetry maps of the upper slope sections of Bilbo Channel and Frodo Channel, respectively. The background bathymetry is a combination of datasets from campaigns CE21015, B2022-18 and B2023-12. The areas covered during the AUV dives are coloured grey. The locations of Figs. 4 to 7 are indicated by black rectangles.

The sediment dynamics in two tributary GCS channels, Bilbo Channel and Frodo Channel (Fig. 1), are the subject of this study. The analysis of channel floor bedforms in their upper slope sections is combined with the bottom current measurements from Verweirder *et al.* (2021) to address the first aim of this study: identifying the main processes (if any) transporting material in the GCS at present, thus testing the (in)activity hypothesis in this land-detached system. Sediment core analysis is used to reach the second aim: testing the presence or absence of sediment transport after the Last Glacial Maximum, thus determining whether the downslope activity of the system displays temporal variability. In doing so, this work intends to improve the understanding of the dynamics in land-detached submarine canyons, as well as their potential consequences, specifically on deep-sea ecosystems. Although there is no one clear definition of what constitutes 'activity' in submarine canyons, here, an active system is referred to as one where gravity flows occur in the present-day environment (cf. Mountjoy *et al.*, 2014; Bernhardt *et al.*, 2015).

SETTING

The study area is situated on the eastern margin of the Porcupine Seabight (Fig. 1). This embayment on the northeast Atlantic margin

originated as a failed rift basin related to the opening of the North Atlantic (Shannon, 1991). It started developing in the Permian, experienced a major rifting episode in the Late Jurassic, and was then subjected to thermal subsidence from the Early Cretaceous onwards (Shannon, 1991; Naylor & Shannon, 2005; Shannon *et al.*, 2007). It has been a continuously open marine environment since the latest Eocene-earliest Oligocene (McDonnell & Shannon, 2001; Stoker *et al.*, 2005), with a present-day maximum water depth of c. 3500 m (Fig. 1A). The GCS is the only large-scale canyon-channel system in the Porcupine Seabight. It stretches for over 200 km and crosses the basin from east to west, connecting the Celtic Sea Shelf to the Porcupine Abyssal Plain (Fig. 1A; Verweirder *et al.*, 2021). During the Quaternary, it is thought to have been draining the periodically ice sheet-covered Celtic Sea Shelf (Tudhope & Scoffin, 1995; Wheeler *et al.*, 2003). In the last glacial cycle, the ice margin of the British-Irish Ice Sheet was closest to the GCS channel heads at about 26 ka, at a distance of c. 50 km (Fig. 1A) (Clark *et al.*, 2022a).

Although the Quaternary glaciations were highly influential in shaping the GCS, the oldest channels of the system were formed before the start of the Quaternary (Verweirder *et al.*, 2023). The first incisions were likely the results of northeast Atlantic margin tilting in the Early Pliocene (Praeg *et al.*, 2005; Stoker *et al.*, 2005; Verweirder *et al.*, 2023). Erosional events caused by the Quaternary glaciations were less severe compared to these initial incisions, but still capable of expanding the GCS with several (smaller) channels and keeping the main channels open.

Over the eastern slope of the Porcupine Seabight, the upper part of the water column below the seasonal thermocline (c. 200 to 700 m water depth) is occupied by Eastern North Atlantic Central Water. The Mediterranean Outflow Water is present underneath, with a high-salinity core at c. 800 to 1000 m water depth (Rice *et al.*, 1991; White, 2007). Both water masses are carried northwards by a general poleward margin flow that is concentrated in the European Slope Current at the continental slope (Pingree & Le Cann, 1990; Rice *et al.*, 1991; White, 2007). A permanent pycnocline is present at about 700 m water depth, at the transition between the two water masses (White, 2007; White & Dorschel, 2010). At this depth, intensification of the tidal bottom currents by freely propagating semi-diurnal or bottom-trapped diurnal internal tides can occur and create a dynamic sedimentary environment (White, 2007; White *et al.*, 2007). As a result, the variability of the Mediterranean Outflow Water's depth and strength is considered the determining factor for the growth and decay of the cold-water coral mounds and associated sediment drift in the Belgica Mound Province (Van Rooij *et al.*, 2007; Huvenne *et al.*, 2009b; Wienberg *et al.*, 2020; Matossian & Van Rooij, 2024).

METHODS

This work is based on two main datasets: (1) data collected in three autonomous underwater vehicle (AUV) dives, and (2) data from two sediment cores. The processing, measurements and analyses performed on these datasets are described below. The two main datasets are complemented by multibeam bathymetry data covering the study area and oceanographic data from a mooring located in Bilbo Channel (Fig. 1B).

Multibeam bathymetry data were acquired in Bilbo and Frodo channels using hull-mounted systems in 2021 (RV Celtic Explorer campaign CE21015), 2022 (RV Belgica campaign 2022-18) and 2023 (RV Belgica campaign 2023-12). The RV Celtic Explorer is equipped with a Kongsberg EM302 1 × 2 degree deepwater multibeam system (30 kHz central frequency), while the RV Belgica is equipped with an EM304 1 × 1 degree system (20 to 32 kHz central frequency). Both vessels are also equipped with high-accuracy Seatex Seapath 330/380 GNSS-IMU systems to provide positioning, motion referencing and timing to the multibeam systems. Regular sound velocity profiles were acquired during these surveys to compensate multibeam data for acoustic refraction. All datasets were processed and cleaned using a combination of CARIS Hips&Sips (Teledyne Technologies, Thousand Oaks (California), USA) and Qimera (QPS, Zeist, The Netherlands) hydrographic processing software following a standard data cleaning approach based on manual editing and automatic filtering of noisy data and outliers. The 2021 dataset was gridded to 15 m horizontal resolution, while the 2022 and 2023 datasets were combined and gridded to 25 m horizontal resolution.

The data from the mooring station in Bilbo Channel are used to validate and quantify the

Table 1. Overview of the three AUV dives where SSS data were collected.

Survey	Start location	End location	Start WD	End WD	Channel	Altitude	Recorded data
1	11°05′2.53″W 50°44′19.69″N	11°14′18.12″W 50°44′19.34″N	373 m	976 m	Bilbo	20 m	LF SSS bathy
2	11°02′22.05″W 50°41′11.79″N	11°08′31.54″W 50°42′18.38″N	486 m	824 m	Frodo	20 m	LF SSS bathy
						8 m	HF SSS LF SSS bathy
3	11°11′10.17″W 50°43′35.19″N	11°14′12.03″W 50°44′21.55″N	858 m	962 m	Bilbo	4 m	HF SSS LF SSS bathy images

bathy, bathymetry; HF, high-frequency; LF, low-frequency; WD, water depth.

results from the AUV data. The mooring data were published in Verweirder *et al.* (2021), but as they are reinterpreted here and integral to the interpretation and discussion of the channel floor processes, a brief overview of the results is presented alongside the results from the AUV data. The mooring sat at 900 m water depth and recorded bottom currents at 8 m above the seafloor between June and mid-December 2005. Further specifics of the mooring setup and processing of the current meter data are described in Verweirder *et al.* (2021).

Combining these four datasets allows for the identification of seabed features on the channel floors and analysis of the processes from which they are generated, as well as their temporal variability. All coordinates, maps and distances are reported based on coordinate reference system WGS84 UTM zone 29N (EPSG: 32629).

AUV data

Decimetre-resolution side-scan sonar (SSS), interferometric bathymetry, and monochrome photography data were collected in three dives during RV Belgica survey 2022-18 using the Flanders Marine Institute AUV Barabas. AUV Barabas is a Gavia AUV from Teledyne and has a depth rating of 1000 m. The AUV is equipped with an inertial navigation system (iXblue C3) aided by a pressure sensor (Keller PA-30X) and a doppler velocity log (Teledyne RDI Pathfinder DVL). Positioning accuracy during the three dives was further improved by mounting an ultra-short baseline (iXBlue Gaps USBL) system on the dropkeel of RV Belgica. For each dive, all raw navigation data were postprocessed using Delph INS Subsea software (Exail Technologies, Paris, France) and exported at 100 Hz. Thus, the navigational error of the postprocessed data was generally kept below 5 m. The operating speed was 1.7 m s^{-1} during all dives, while other operational settings were adjusted for each dive individually (Table 1).

Side-scan sonar

SSS data were collected using a Klein 3500 module operating either in 455 kHz low-frequency (LF) or 900 kHz high-frequency (HF) mode (Table 1). Processing included updating the real-time positioning data in the sonar files with the postprocessed navigation data, which was carried out using NavInjector Pro software (Chesapeake Technology, New York (New York), USA). Then, the data were postprocessed and compiled into mosaics using SonarWiz software (Chesapeake Technology, New York (New York), USA). Postprocessing steps were tailored to each dataset and included a nadir transparency filter, empirical gain normalisation, heading and pitch correction, and, when necessary, a destriping filter. Turns in the AUV track were not included in the final mosaic as they contained distorted data. The LF data were gridded to a resolution of 0.25 m, while the HF data were gridded to a resolution of 0.10 m.

Bathymetry

Along with the LF SSS data, the Klein 3500 module is capable of recording bathymetry through interferometry. After correcting the navigation information in the raw SSS files, the

Klein Batch Processing software (Klein Marine Systems, Newburyport (Massachusetts), USA) was used to transfer the raw transducer stave data into raw bathymetry data that are readable by commercial processing software. During post-processing in SonarWiz software, the data were corrected for variable sound velocity in the water column obtained through the AUV's onboard sound velocity sensor (Valeport miniSVS), and filters were applied to remove faulty near-range values in the nadir. Afterwards, the bathymetry point cloud was loaded into AutoClean software (BeamworX, Utrecht, The Netherlands) and more faulty pings were removed with filters and, where necessary, manually. All AUV bathymetry data were gridded to a resolution of 0.5 m.

After processing, the qProf plugin in QGIS was used to construct bathymetry profiles. Bedform crests and troughs were determined visually from the profiles. Bedform morphometries were determined following the method used in Lo Iacono *et al.* (2020). Wave heights and wavelengths were calculated as the perpendicular distance from the crest to the bedform baseline, and the distance along the baseline between two consecutive wave troughs, respectively (Fig. 2). The asymmetry index (AI) is the ratio of the difference of the distances between the crest and the upslope and downslope troughs, and the wavelength (Fig. 2). Bedforms with AI values between −0.2 and 0.2 are considered symmetric, while more negative or positive values indicate upslope or downslope asymmetry, respectively.

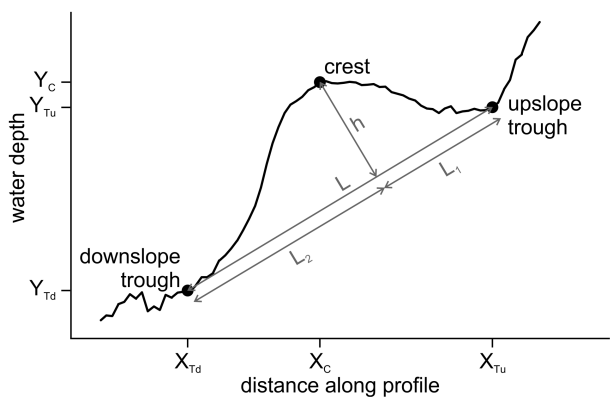

Fig. 2. Sketch depicting the method for calculating the bedform morphometries: wave height (h), wavelength (L) and asymmetry index (AI = (L1-L2)/L) (Lo Iacono *et al.*, 2020).

Photography

During several sections of the AUV dives, the altitude above the seafloor was low enough to enable seafloor photography using the camera in the nose section of the AUV (Grasshopper GRAS-14S5M-C) (Table 1). Pictures were taken at a framerate of 3.75 frames per second. The images were loaded into QGIS by applying the navigation information from the AUV (altitude, depth, heading, latitude, longitude, pitch) and calculating the image size from the flying altitude and a seawater refraction index of 1.33 (calculated according to Quan & Fry, 1995) to ensure correct scaling and measurements of any features.

Sediment cores

Two sediment gravity cores (B2306-GC02 and B2306-GC04) were collected from the floor of Bilbo Channel during RV Belgica survey B2023-12 (Table 2). They were cut into 1 m-sections, capped and labelled on the ship.

Computed Tomography (CT) scanning was performed on whole cores using the Siemens medical CT scanner at Ghent University Hospital in Belgium. Dragonfly software was used for visualisation and basic analysis of the data. After opening, the cores were photographed at Ghent University using the linescan camera incorporated in the GeoTek multi-sensor core logger (MSCL) system. The MSCL-Standard of Ghent University was also used to measure the gamma-ray density, magnetic susceptibility (point sensor) and colour spectrum (reflectance, XYZ, $L^*a^*b^*$) at 0.5 cm resolution. Afterwards, the cores were described visually for their lithology, colour and structures.

Based on the CT images, visual description and geophysical datasets, the cores were sampled for grain size analysis. Following the method described in Wils *et al.* (2021), a chemical pretreatment was used to isolate the terrigenous fraction from the samples by boiling the samples in 10 ml DI water with H_2O_2 (2 ml, 35%), HCl (1 ml, 10%) and NaOH (1 ml, 2 M) to remove organic matter, calcium carbonate and biogenic silica, respectively. Lastly, samples were boiled with sodium hexametaphosphate (1 ml, 2%) to ensure disaggregation of the particles. Grain size analysis was performed using the Malvern Mastersizer 3000 laser diffraction particle size analyser at Ghent University. Each sample was measured thrice to ensure robustness and reproducibility of the results. The

Table 2. Details of the sediment cores used in this study.

Core name	Type	Latitude	Longitude	WD (m)	Setting	Length (m)
B2306-GC02	Gravity	50°42.155′N	11°24.488′W	1612	Channel floor	2.99
B2306-GC04	Gravity	50°41.664′N	11°31.853′W	1827	Channel floor	3.00

WD, water depth.

average distribution of each triplicate was used in further analysis.

Mixed planktic foraminifera were collected from the >150 μm fraction of a total of five 1 cm-thick intervals over the two cores. Samples were sent to Beta Analytic (Miami, USA) for accelerator mass spectrometry radiocarbon analysis. The rbacon package (v3.3.1; Blaauw & Christen, 2011) was used to construct Bayesian age models for both cores from their respective radiocarbon ages, which were calibrated using the Marine20 calibration curve (Heaton *et al.*, 2020) and $\Delta R = 0$, as per the protocol established by the BRITICE-CHRONO project (Clark *et al.*, 2022b) (Supplementary Material S1). Ages for specific horizons mentioned in the text and figures refer to median ages extracted from the model at the respective depths.

Both cores were scanned for their geochemical properties using an ITRAX machine at the Austrian Core Scanning Facility of the University of Innsbruck (Supplementary Material S2). Selected core intervals were measured thrice to test robustness and reproducibility and only elements where the Pearson correlation coefficient (r) for the repeated measurements was 0.75 or higher were included in the analysis: Si, K, Ca, Ti, Fe, Rb, Sr, Zr and Ba. For each core, the element intensities (in counts per second; cps) were centre-log transformed to reduce the unwanted effects of physical properties and matrix effects on the data (Bertrand *et al.*, 2024). Furthermore, a partial least squares regression was performed on a subset of elements (Si, K, Ti, Fe, Rb and Zr) to predict mean grain size at the resolution of the XRF measurements (0.2 mm) across the full depths of both cores. In this procedure (Supplementary Material S2), the method described in Liu *et al.* (2019) was implemented in R using the pls package (v2.8-5) (Mevik & Wehrens, 2007).

RESULTS

The multibeam bathymetry data show that the upper slope sections of Bilbo and Frodo channels have U-shaped cross-sectional geometries with flanks of 200 to 400 m high, and channel floors that are about 1.5 km and 0.8 km to 1.2 km wide, respectively. Their northern flanks are slightly steeper than the southern flanks and their floors dip downslope at an average angle of 2.2° (Fig. 1B). The mooring data, data from the AUV dives and sediment core data are described in more detail below.

Bottom currents

Present-day bottom currents in the GCS have speeds that are on average 15.1 cm s^{-1} and reach maximum values of 53.7 cm s^{-1} (Fig. 3). The current meter record is dominated by tidal currents: the M_2 (principal lunar semidiurnal; 12.42 h period), S_2 (principal solar semidiurnal; 12 h period) and K_1 (lunar diurnal; 23.93 h period) tidal ellipses are all oriented parallel to the channel axis (E-WNW) (Fig. 3). This results in a continuous up- and downslope movement of the bottom currents in Bilbo Channel (Verweirder *et al.*, 2021). The overall residual current is oriented towards 324°N (≈ NW) with a speed of 4.75 cm s^{-1}.

Channel floor bedforms and structures

Channel head gullies

Down channel-oriented gullies were observed in the head of both channels. They are most pronounced in Frodo Channel, where they form a dendritic network (Fig. 4A, B). They are 10 to 25 m deep, 100 to 200 m wide and are identified down to water depths of about 750 m. Some gullies (Fig. 4B, D) are recognised as areas of higher backscatter intensity in the SSS data, indicating an increased roughness of the seabed there compared to the surrounding channel floor. Most gullies, however, have a SSS intensity that is similar to the surrounding seabed (Fig. 4B).

The gullies in Bilbo Channel were not covered during the AUV dives. The SSS data just downslope of where they are located, however, display high-reflectivity linear features (ripples?) that are in line with the upslope gullies (Fig. 4E).

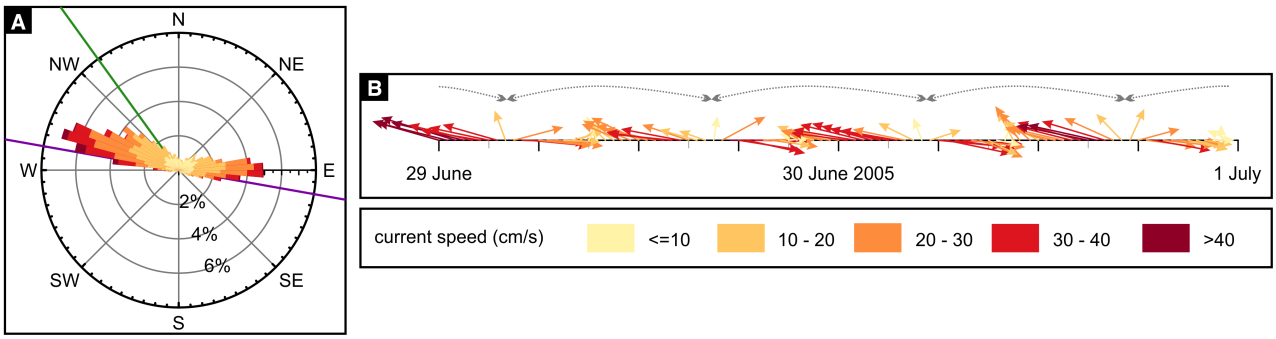

Fig. 3. (A) Rose diagram showing the bottom current directions and speeds as a percentage of the total number of measurements recorded by the mooring in Bilbo Channel described in Verweirder *et al.* (2021) (for location, see Fig. 1). The orientation of the Bilbo Channel axis is indicated in purple. The direction of the overall residual current is indicated in green. (B) Vector diagram showing a representative two-day time series of current directions and speeds just after spring tide. The grey arrows indicate semi-diurnal cyclicity.

In one of the gullies in the head of Frodo Channel, a train of wavy bedforms was identified. They are crescentic in shape with heights of 1 to 2 m and wavelengths of 10 to 15 m (Fig. 4C). Another section of this gully further downslope contains two scarps that are each about 1 m high (Fig. 4D).

Wavy bedforms

Wavy bedforms were identified on the channel floors of both channels, in water depths of 840 to 885 m (Bilbo Channel) and 750 to 850 m (Frodo Channel) (Figs. 5 and 6). Based on their dimensions (Table 3), they are classified as megaripples (van Dijk *et al.*, 2020). The megaripple crests are straight to sinuous and some have developed bifurcation (Fig. 5). Most megaripples in Bilbo Channel are symmetric. About a third of the measured bedforms is downslope asymmetric, whereas upslope asymmetry is rare (Fig. 5B). The gentler (stoss) side of the asymmetric megaripples is characterised by higher backscatter compared to the steeper (lee) side (Fig. 5A). In Frodo Channel, ripplefield A is characterised by megaripples with upslope asymmetry (Fig. 6C) and stoss sides that have a lower intensity in the SSS data (Fig. 6B). The megaripples in ripplefield B, on the other hand, are mostly symmetric or downslope asymmetric and upslope asymmetry is rare (Fig. 6C). There is no difference in backscatter character for either flank (Fig. 6B).

In the photographs, smaller ripples were identified superimposed on the Bilbo Channel megaripples (Fig. 5C). They have wavelengths of about 20 cm and their straight to sinuous crests are oriented parallel to the crests of the megaripples. Wave heights cannot be measured from the top-down photographs, but the ripples do look most pronounced when located on a megaripple crest. They often disappear for 0 to 5 m just over the crest on the megaripples' lee side, after which they show up again over the remainder of the lee side, the megaripple trough and the stoss side of the next megaripple (Fig. 5C, Supplementary Material S3).

Fig. 4. Close-up maps showing gully features in Frodo (A)–(D) and Bilbo (E) channels. Yellow dotted lines indicate the locations of gullies. In SSS data, whiter values indicate higher backscatter intensities. The background bathymetry is the 25 m-grid from the RV Belgica 2022-18 and 2023-12 campaigns, from which depth contours were extracted every 25 m and indicated in black. (A) Bathymetry and (B) low-frequency SSS data in the head of Frodo Channel. The location of Fig. 4C is indicated by a black/white rectangle. (C) Close-up of the low-frequency SSS data in (B) (left) and their interpretation (right). A train of dunes and potential ripples are indicated in white. The inset shows a bathymetry profile through the train of dunes. (D) Low-frequency SSS data showing a section of a gully in Frodo Channel between c. 650 and 730 m water depth (upper panel) and its interpretation (lower panel). Cold-water coral mini-mounds are indicated with green arrows, and three scarps are indicated as pink dashed lines. (E) Low-frequency SSS data of Bilbo Channel between c. 600 and 740 m water depth (left) and their interpretation (right). Features (ripples?) at the downslope extent of this gully are indicated in white.

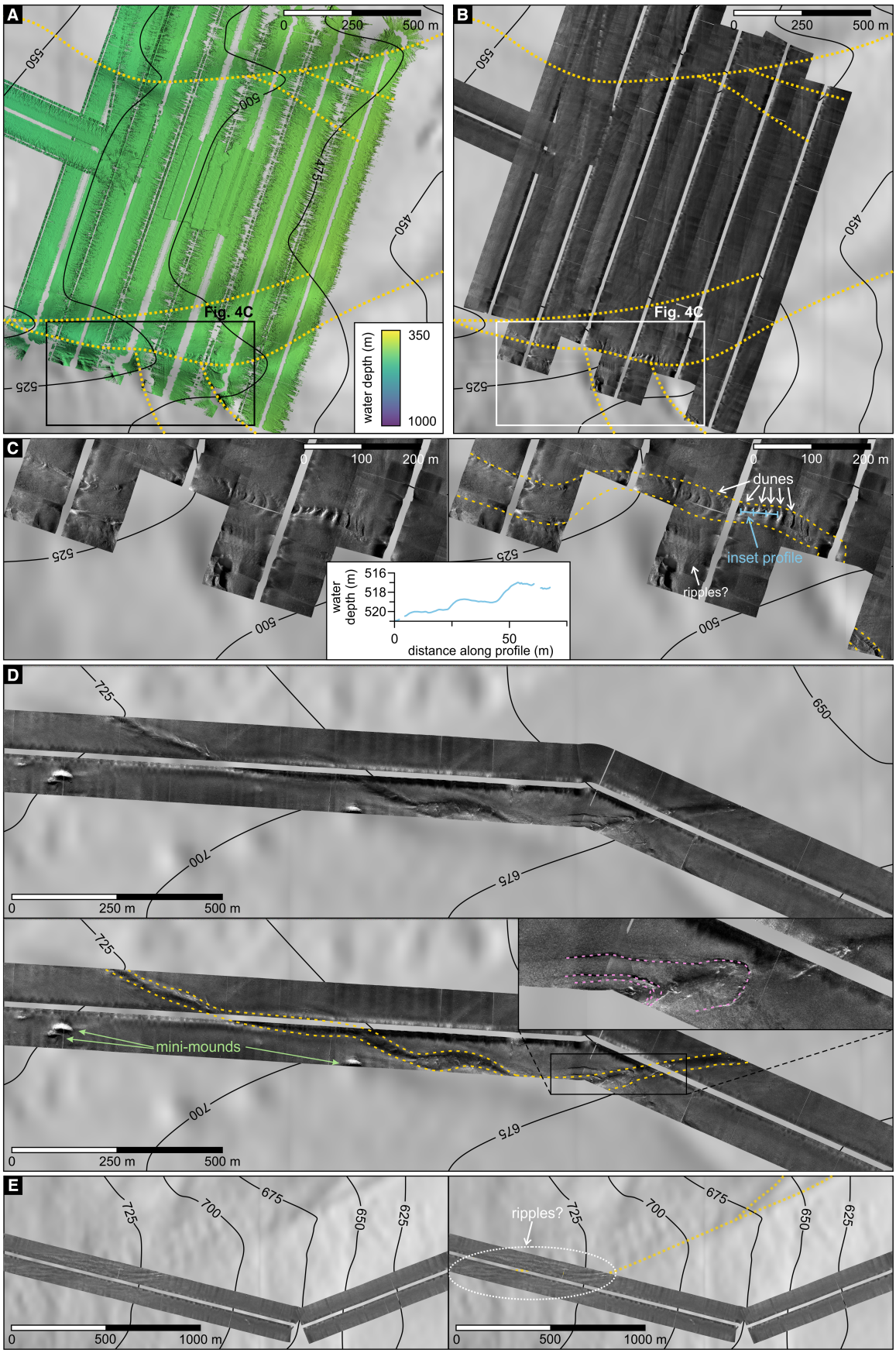

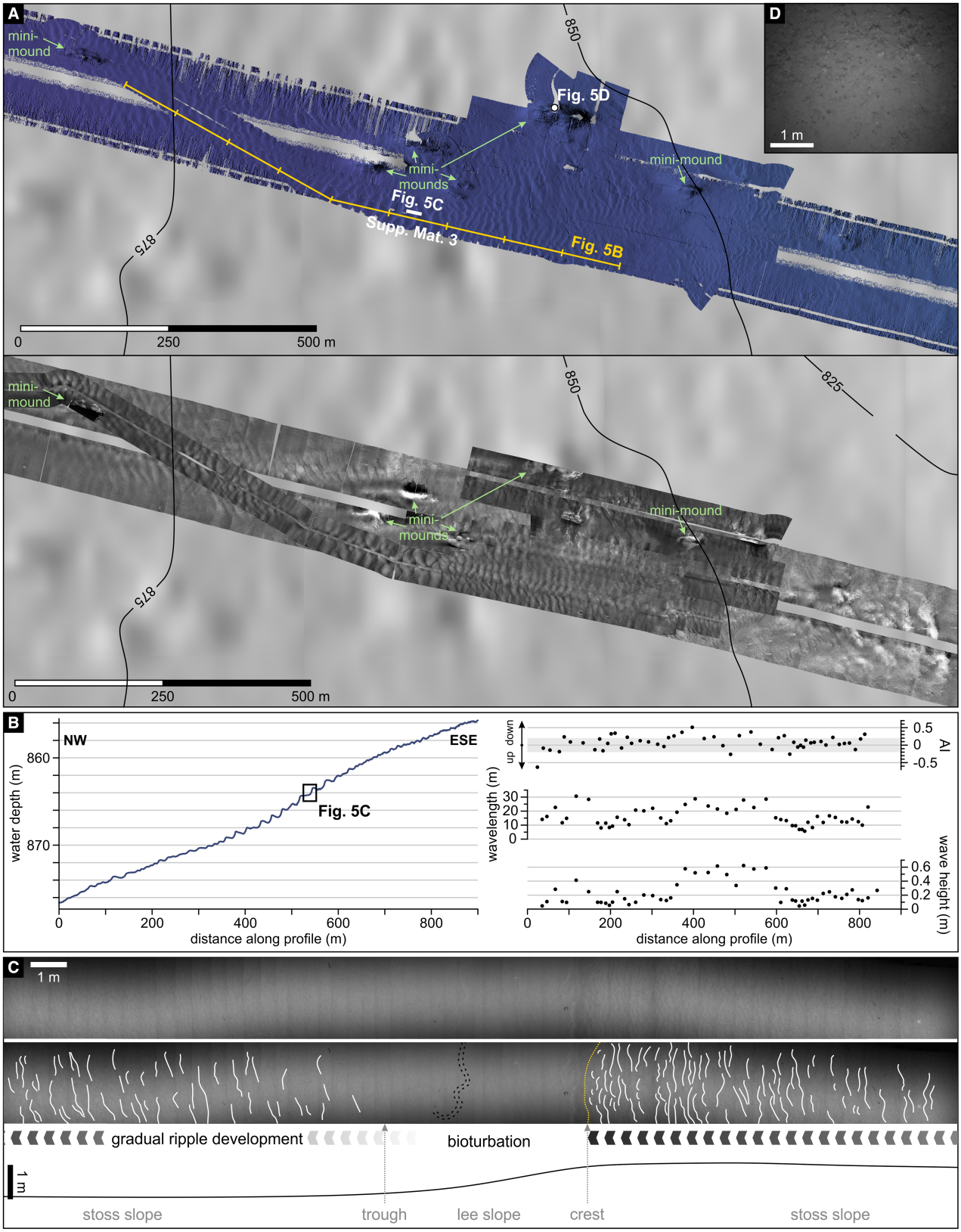

Fig. 5. (A) Close-up map showing AUV bathymetry of the Bilbo Channel axis between 830 m and 880 m water depth. A field of megaripples is visible, as well as cold-water coral mini-mounds indicated by green arrows. The bathymetry profile shown in (B) is indicated in yellow, with markers every 100 m. The strip of images shown in (C) and in Supplementary Material S3 is indicated as a white rectangle. The location of the photograph in (D) is indicated as a white dot. The background bathymetry is the 25 m grid from the RV Belgica 2022-18 and 2023-12 campaigns, from which depth contours were extracted every 25 m and indicated in black. (B) Graphs showing the water depth of the bathymetry profile indicated in (A), and the wave height, wavelength and asymmetry index (AI) of the megaripples it crosses. Megaripples of AI between −0.2 and 0.2 (indicated in grey) are considered symmetric. (C) A strip of stitched-together monochrome images recorded by the AUV over the megaripple field in Bilbo Channel (upper panel) and their interpretation (lower panel). The interpreted figure shows superimposed ripple crests in white, a megaripple crest in yellow, and a track produced by deep-water fauna in black. (D) Black-and-white photograph over the flank of one of the cold-water coral mini-mounds.

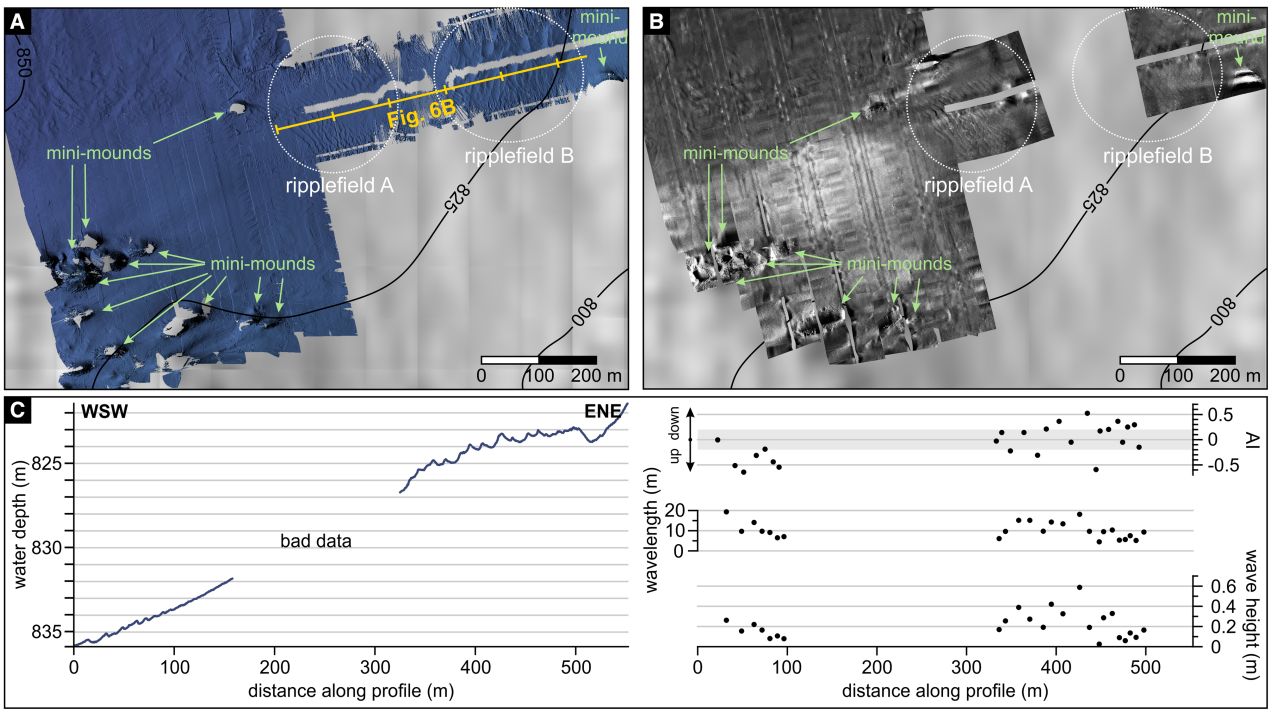

Fig. 6. Close-up maps showing AUV bathymetry (A) and low-frequency SSS (B) of the Frodo Channel axis between c. 820 m and 850 m water depth. In the SSS data, whiter values indicate higher backscatter intensities. Two fields of megaripples are indicated in white, and cold-water coral mini-mounds are indicated by green arrows. The bathymetry profile shown in (C) is indicated in yellow, with markers every 100 m. The background bathymetry is the 25 m-grid from the RV Belgica 2022-18 and 2023-12 campaigns, from which depth contours were extracted every 25 m and indicated in black. (C) Graphs showing the water depth of the bathymetry profile indicated in (A), and the wave height, wavelength and asymmetry index (AI) of the megaripples it crosses. Megaripples of AI between −0.2 and 0.2 (indicated in grey) are considered symmetric.

Cold-water corals

In the bathymetry data, mounded features are identified in water depths of 840 to 1000 m and 680 to 840 m in Bilbo and Frodo channels, respectively (Figs. 5 and 6, respectively). They are oblong structures oriented along the channel axis that are on average 56 m long, 27 m wide, and 7 m high (ranges 30 to 105 m, 12 to 48 m and 2 to 17 m, respectively). Their backscatter character shows high reflectivity in the SSS data, indicative of coarse texture (Figs. 6 and 7). The seabed photos show that these are cold-water coral mounds (Fig. 7D to G, Supplementary Material S4). Based on their

Table 3. Dimensions of the megaripples in Bilbo and Frodo channels shown as [average (minimum; maximum)].

Channel	Wavelength (m)	Wave height (cm)	Crest orientation	AI
Bilbo	15.9 (5.7; 30.6)	23 (5; 62)	N-S	0.1 (−0.6; 0.5)
Frodo	10.2 (4.5; 19.3)	21 (3; 59)	N-S/NNW–SSE	−0.1 (−0.6; 0.5)

AI, asymmetry index.

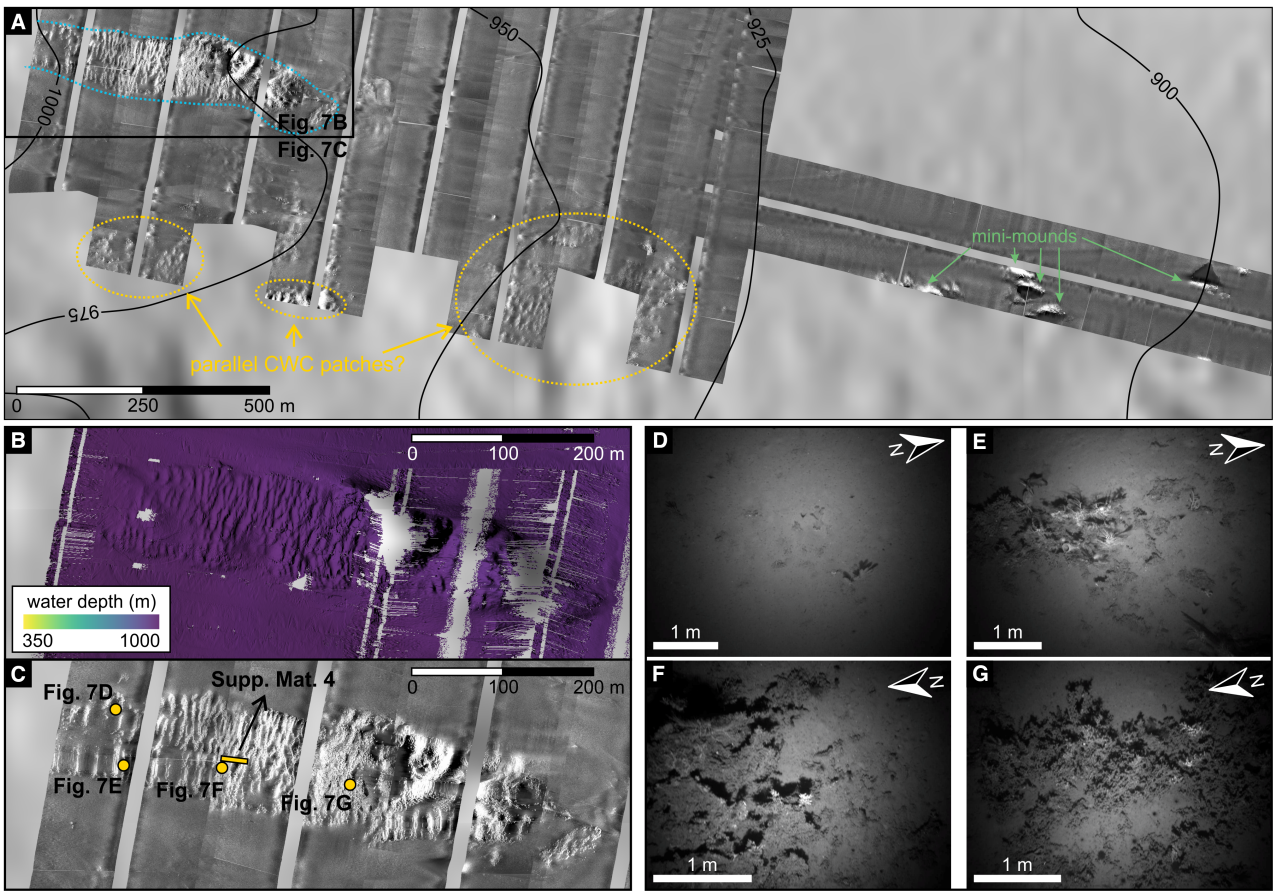

Fig. 7. (A) Close-up map showing low-frequency SSS data of the Bilbo Channel axis between c. 890 m and 1000 m water depth. Whiter values indicate higher backscatter intensities. A large cold-water coral structure is indicated in blue; cold-water coral mini-mounds are indicated by green arrows; lined-up parallel cold-water coral patches are indicated in yellow dotted circles. The location of Fig. 7B, C is indicated as a black rectangle. The background bathymetry is the 25 m-grid from the RV Belgica 2022-18 and 2023-12 campaigns, from which depth contours were extracted every 25 m and indicated in black. (B) AUV bathymetry of the large cold-water coral mound in Bilbo Channel. (C) Low-frequency SSS of the large cold-water coral mound in Bilbo Channel. Whiter values indicate higher backscatter intensities. The locations of the images shown in (D)–(G) as well as the strip of images used in Supplementary Material S4 are indicated in yellow. (D)–(G) Monochrome images recorded by the AUV flying over the large coral mound shown in (B) and (C).

dimensions, they are called mini-mounds, similar to examples from other locations (Masson *et al.*, 2003; Foubert *et al.*, 2011; Stewart *et al.*, 2014; Collart *et al.*, 2018). In the black-and-white images, white parts of the coral framework are interpreted as living coral, whereas the darker (greyer) parts are interpreted as dead framework or rubble (Hebbeln *et al.*, 2014).

Table 4. Results of the AMS radiocarbon analysis, with conventional radiocarbon ages given alongside the calibrated ages reported as [average (95% range minimum – 95% range maximum)].

Lab code	Core	Depth (cm)	Material	Analysed weight (mg)	^{14}C age (yr BP)	Calibrated age (cal yr BP)
Beta - 699 043	B2306-GC02	78–79	Mixed planktic foraminifera	5.9	2810 ± 30	2410 (2172–2674)
Beta - 699 044	B2306-GC02	237–238	Mixed planktic foraminifera	5.1	8370 ± 30	8760 (8526–9005)
Beta - 699 045	B2306-GC04	104–105	Mixed planktic foraminifera	4.8	5720 ± 30	5959 (5703–6236)
Beta - 699 046	B2306-GC04	168–169	Mixed planktic foraminifera	8.6	14 540 ± 40	16 485 (15521–16 928)
Beta - 699 047	B2306-GC04	232–233	Mixed planktic foraminifera	9.4	17 300 ± 50	19 860 (18891–20 379)

At c. 1000 m water depth in Bilbo Channel, a considerably bigger coral structure is present (Fig. 7A to C). It is elongated along the channel axis, c. 600 m long, a little over 100 m wide and about 30 m high. The corals in this particular structure are organised in subparallel patches oriented perpendicular to the channel axis (north–south). The patches are c. 0.4 m high and spaced about 9.8 m apart on average (ranges 0.1 to 1.3 m and 4.4 to 20.1 m, respectively).

Additional parallel, coarse-textured, high-backscatter areas are present on the southern edge of the SSS data in Bilbo Channel (c. 930 to 985 m water depth; Fig. 7A). They are recognised as elevated areas in the bathymetry data. As they were only partially covered by the AUV data, however, extracting any meaningful dimensions is not possible.

Sediment cores

The results of the accelerator mass spectrometry analysis are given in Table 4. The two samples in core B2306-GC02 are of Holocene age. In core B2306-GC04, the deepest sample has a Last Glacial Maximum age, while the middle sample was formed during the last deglaciation, and the youngest sample has a Holocene age.

B2306-GC02

The bottom interval (299 to 275 cm) in core B2306-GC02 has a very dark greyish brown colour and appears chaotic, with a grey (very dark greenish grey) mud clast and dipping laminations (inset Fig. 8). Shell fragments are present as well, and this section is bioturbated. According to the age model, the age at the top of the disturbed interval is c. 10 400 cal yr BP (Fig. 8). From 275 to 254 cm core depth, <1 mm to 1 cm thick intervals with distinct upper and lower boundaries are visible both to the naked eye, as darker (very dark grey) and coarser sections than the background mud, and in the CT scan as sections of higher intensity. They have a very fine sand lithology with a fining-upward trend in the thickest layers (Fig. 8) and most layers are deformed or interrupted by bioturbation. The three thickest layers can each be correlated with a peak in magnetic susceptibility and density values, as well as increased Zr, Si, Ca and Sr values in the XRF data (Fig. S1). According to the age model, the uppermost layer was deposited c. 9600 cal yr BP (Fig. 8). Most of the core (254 to 8.5 cm core depth) consists of bioturbated foraminifera-rich silt (Fig. 8). Within this unit, the colour gradually changes from dark grey at the bottom to dark greyish brown, greyish brown and finally light brownish grey at the top. The upper 2.5 cm of core B2306-GC02 (8.5 to 6 cm core depth) are greyish brown in colour, with an orange hue, and are silty with a fine sand component.

B2306-GC04

At the bottom of the core, between 290 cm and 172 cm core depth, core B2306-GC04 is characterised by horizontal to distorted and dipping layers, with pieces of gravel scattered throughout. Most of the layers are c. 1 mm to several millimetres in thickness and, where visible to

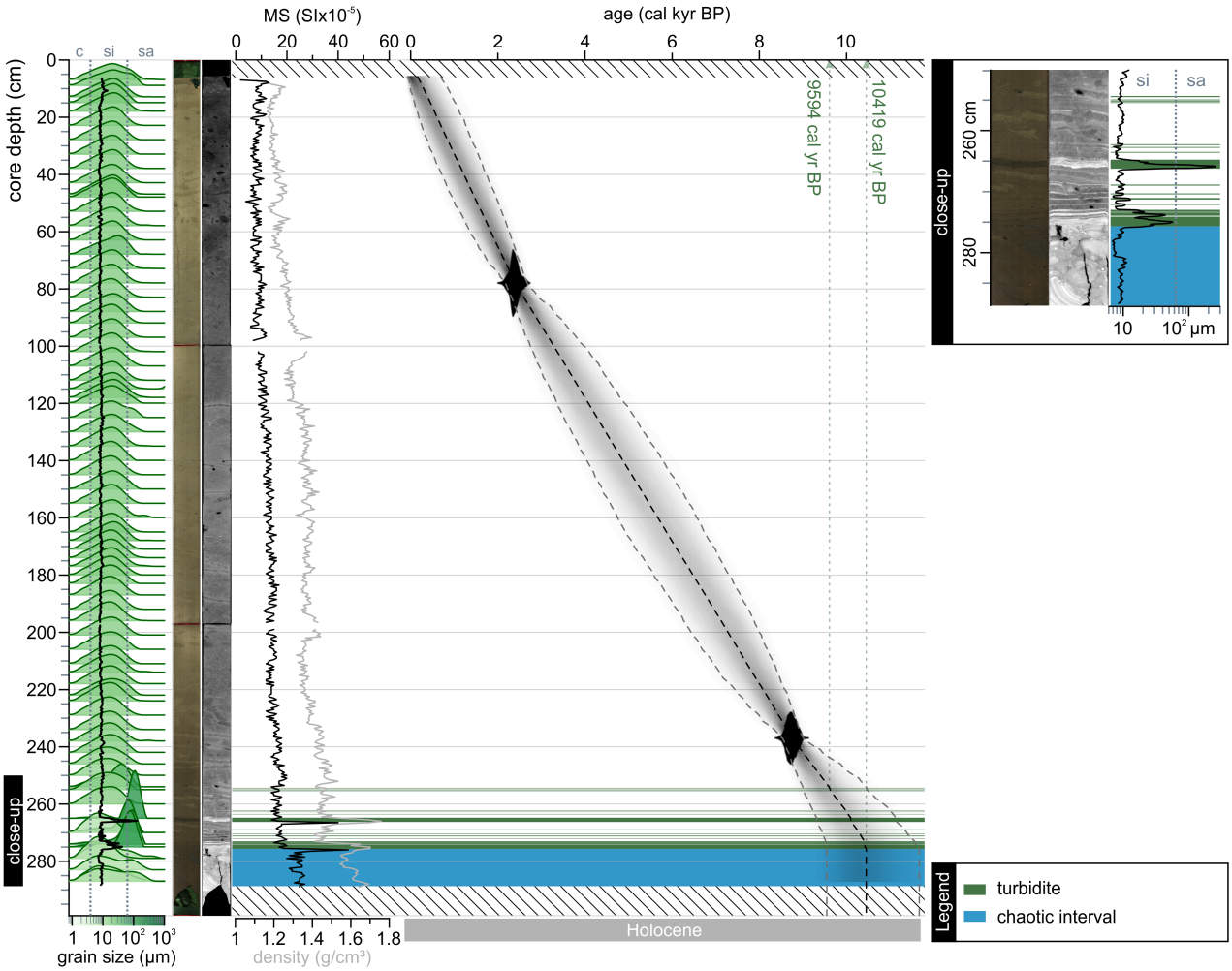

Fig. 8. Core B2306-GC02. From left to right: grain size distribution plots coloured according to the mode (with darker green representing a coarser mode) and mean grain size predicted from XRF data plotted in black; core photograph; CT scan; magnetic susceptibility; gamma-ray density; age-depth model. The inset represents a close-up of the photograph, CT scan, predicted mean grain size and identified facies for the 250 to 289 cm interval.

the naked eye, sandier and darker coloured than the background sediment, except for two greenish grey layers at 262 to 260 cm and 177 cm core depth (Fig. 9). These two layers have very slightly coarser lithologies and coincide with peaks in the Ca curve and dips in the magnetic susceptibility data (Fig. 9). The other layers have varying characteristics in the magnetic susceptibility, density, CT, or XRF data (Fig. 9, Fig. S2). The interval at the very bottom (290 to 263 cm) appears chaotic. Above the layered interval, a structureless very dark greyish brown silty sand crosscut by four burrows is present between 172 cm and 161 cm core depth. It transitions into a chaotic-looking sandy silt interval (161 to 152 cm core depth; inset Fig. 9) that contains pieces of gravel and sediments of grey, black, beige and brown colours in distorted layers, and is capped by a layer of very fine sand. At 152 cm core depth, a distinct but irregular erosional boundary is present that represents a hiatus of c. 5300 years between c. 16.0 and c. 10.7 cal kyr BP (Fig. 9). The upper part (152 to 0 cm core depth) of core B2306-GC04 is made up of bioturbated foraminifera-rich beige silt (Fig. 9). Within this section, the colour changes from dark greyish brown at 152 cm core depth to greyish brown, grey, and eventually light brownish grey at the top of the core.

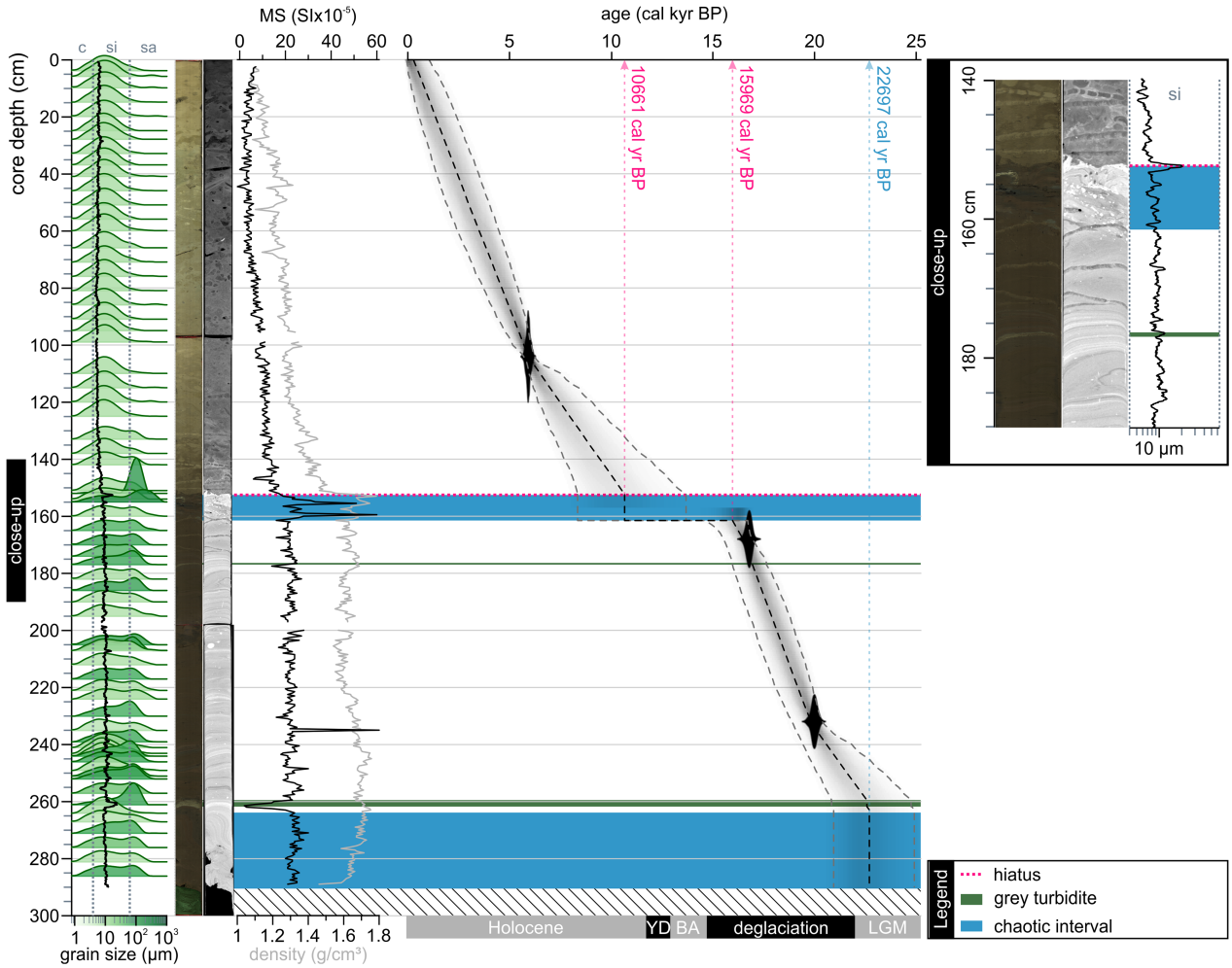

Fig. 9. Core B2306-GC04. From left to right: grain size distribution plots coloured according to the mode (with darker green representing a coarser mode) and mean grain size predicted from XRF data plotted in black; core photograph; CT scan; magnetic susceptibility; gamma-ray density; age-depth model. The inset represents a close-up of the photograph, CT scan, predicted mean grain size and identified facies for the 140 to 190 cm interval. YD, Younger Dryas; BA, Bølling-Allerød; LGM, Last Glacial Maximum according to Clark *et al.* (2022b).

DISCUSSION

Present-day predominance of tidally modulated bottom currents

Indications from (mega)ripples

The Bilbo Channel current meter (for location, see Fig. 1) recorded tidally modulated bottom currents that are strongly oriented along the channel axis (E-WNW) and, therefore, perpendicular to the N-S orientation of the megaripple crests in both channels and the N-S orientation of the superimposed ripples in Bilbo Channel (Figs. 3 and 5). Flume tank experiments in which a unidirectional current (or combined wave-current regime) is imposed onto an initial setup of a flat, sandy bed for a prolonged time (several hours) result in an equilibrium configuration where large-scale (asymmetric) wavy bedforms (bars, sandwaves or dunes) are covered by superimposed ripples and both the primary structures and the superimposed ripples have crests perpendicular to the flow direction (Catañ o-Lopera & García, 2006). The symmetric to slightly downslope-asymmetric geometries of most of the megaripples observed here (Figs. 5 and 6) suggest that the bidirectional current action oriented along the channel axis is influential for megaripple geometry (Cataño-Lopera & García, 2006). Considering that the channel floor sediments are mostly silty sands (Tudhope & Scoffin, 1995), the measured bottom current

velocities are capable of transporting the channel floor sediments (Stow *et al.*, 2009) and building the straight to undulatory ripples visible in the AUV images (Fig. 5). The superimposed ripples are likely the ripples that Tudhope & Scoffin (1995) observed during their submersible dives and attributed to reversing bottom currents. Higher energies are probably required for megaripple formation and migration (Passchier & Kleinhans, 2005; Stow *et al.*, 2009; Foubert *et al.*, 2011; Lo Iacono *et al.*, 2020). This implies temporal variations in the sediment dynamics in the channels, where the megaripple fields are formed and active only during periods of peak velocities of the tidal bottom current. Small-scale spatial variations, on the other hand, are suggested by the upslope-asymmetric megaripples in ripplefield A, which likely represent a local phase of strengthened up-canyon currents and sediment transport.

Despite the current measurements suggesting that the megaripples were not actively migrating during the measurement period (cf. Stow *et al.*, 2009), the present-day channel floors can be considered a dynamic environment. Tudhope & Scoffin (1995) noticed formation of new ripples in Bilbo Channel during an experiment that spanned a period of 21 days. Active migration of the superimposed ripples is also supported by the current meter measurements and the ripples distribution pattern over the megaripples presented here. The superimposed ripples are larger and more abundant on the megaripples crests than in the troughs and may be absent on the megaripples lee sides (Fig. 5C). This is consistent with the SSS intensities increasing crestwards over the megaripples stoss sides and lower intensities on their lee sides. This pattern has been recognised in both experimental and field data (Cataño-Lopera & García, 2006; Li & King, 2007; Guerrero & Guillén, 2020) and is caused by the topography of the primary bedform producing a larger velocity over its crest (Cataño-Lopera & García, 2006). Flow separation may occur over the crest of the primary bedform depending on the lee side angle (Kwoll *et al.*, 2016; Zomer *et al.*, 2021), leading to the creation of a high-turbulence, low-horizontal velocity eddy and the absence of bedforms there (Venditti *et al.*, 2005; Naqshband *et al.*, 2014; Herbert *et al.*, 2015). Superimposed bedforms are known to contribute to the growth and migration—and, therefore, maintenance—of their primary bedform (Venditti *et al.*, 2005; Reesink & Bridge, 2007, 2009). As the superimposed ripples migrate over the stoss side of the primary bedform, they eventually reach its crest and produce grain flows over its lee side. Therefore, migration of the superimposed ripples in the study area facilitates (slow) migration of the megaripples.

The downslope asymmetry of the superimposed ripples may be explained by the asymmetry in the bottom current direction and strength. About 40% of all current measurements were oriented towards the west to northwest (downslope), while about 30% were directed towards the ESE to ENE (upslope) (Fig. 3). Additionally, over 70% of the currents with speeds >30 cm s^{-1} were directed downslope (Fig. 3). However, current intensities in the Porcupine Seabight are known to experience seasonal differences in strength (Rice *et al.*, 1991). Thus, the current meter record of the Bilbo Channel mooring is potentially not long enough to capture the full cycle of current variations, and the asymmetry in bottom current direction and strength might even itself out over time. Tudhope & Scoffin (1995) observed both upslope- and downslope asymmetrical ripples, as well as symmetrical and interference ripples. This variation in geometries suggests that small-scale processes may determine the (a)symmetry of the superimposed ripples.

Indications from cold-water corals

Based on their dimensions, the oblong structures containing cold-water corals observed in Bilbo Channel and Frodo Channel are classified as cold-water coral mini-mounds such as those reported as part of the Belgica Mound Province (Moira Mounds; Foubert *et al.*, 2011), on the interfluves next to the Explorer and Dangeard canyons in the upper reaches of the Whittard Canyon System (Stewart *et al.*, 2014), surrounding the head of Ferrol Canyon on Ortegal Spur (Collart *et al.*, 2018), as part of the Darwin mound area in the northern Rockall Trough (Masson *et al.*, 2003; Huvenne *et al.*, 2009a), in the Mingulay Reef Complex (De Clippele *et al.*, 2017), in the Træna Deep Coral reef field (Cathalot *et al.*, 2015), on Galicia Bank (Somoza *et al.*, 2014), offshore Morocco (Glogowski *et al.*, 2015), and on Great Bahama Bank (Correa *et al.*, 2012). They tolerate a large range of oceanographic conditions and their occurrence seems mainly controlled by food supply, which in turn depends on primary production near the water surface and processes that bring the food particles to the corals living at greater water depths

(Freiwald *et al.*, 2004; Duineveld *et al.*, 2007; Wienberg & Titschack, 2015; Hennige *et al.*, 2021). The very high-resolution AUV data presented here allow us to observe these structures both in detail and within their channel floor context for the first time. Tudhope & Scoffin (1995) observed small (0.1 to 1.0 m) colonies of living corals and patches of dead corals (c. 25 m diameter) in their submersible dives in Bilbo Channel but do not mention any mounded structures. Within canyon-channel systems, (framework-forming) cold-water corals are often found as patches or communities on steep and/or rocky outcrops in canyon flanks (Mortensen & Buhl-Mortensen, 2005; Orejas *et al.*, 2009; Tyler *et al.*, 2009; De Mol *et al.*, 2011; Huvenne *et al.*, 2011; Morris *et al.*, 2013; Brooke & Ross, 2014; Sánchez *et al.*, 2014), and rarely, as seen here, in mounded structures on the channel floor (Sánchez *et al.*, 2014). Rocky canyon walls provide hard substrates for settling and intersect with the dilute sections of gravity currents that provide food particles and where energies are not so high that they sweep away any growing colonies (Huvenne *et al.*, 2011). The channel floors of the GCS are littered with dropstones from Quaternary glaciations (Tudhope & Scoffin, 1995) that can serve as points for settling and initial attachment of coral polyps (Huvenne *et al.*, 2005; Roberts *et al.*, 2006). The presence of living sections of coral (Fig. 7) suggests the absence of erosive gravity currents in that part of the channel at present.

Coral growth is further aided by the oceanographic conditions. The depth interval at which the mini-mounds occur in the GCS (c. 700 to 1000 m) corresponds to the water depths where the upper part of the Mediterranean Outflow Water is situated and transitions into the Eastern North Atlantic Central Water above. At these depths in the Belgica Mound Province further north in the basin (Fig. 1A), large-scale cold-water coral mounds are present in dynamic bottom current regimes created by bottom trapped diurnal waves rectified by the topography (Rice *et al.*, 1991; White & Dorschel, 2010; Wienberg *et al.*, 2020). Similarly, bottom currents are here suggested to create favourable conditions for settling and growth of the cold-water corals observed in the GCS channel axes. Settling substrates such as hardgrounds, dropstones or coral rubble are often created or maintained by enhanced bottom currents. The bottom currents also prevent any (hemi)pelagic sediments from draping over them. Once settled, the filter-feeding corals need a steady supply of food particles to grow (Dullo *et al.*, 2008). Here, a consistent transport of particles over the seafloor is likely promoted by the continuous up- and downslope movement of the bottom currents. These currents may also prevent sediment from accumulating on and burying the corals. Although it is possible that the bottom currents (with semi-diurnal signal) originate from the freely propagating internal waves that are present at the interface between the Eastern North Atlantic Central Water and the Mediterranean Outflow Water (e.g. Mulder *et al.*, 2012; Aslam *et al.*, 2018; Antsey *et al.*, 2024), further measurements should be undertaken to verify this hypothesis.

Typically, in an environment dominated by a unidirectional bottom current, cold-water coral mounds and patches tend to grow into the dominant current, which often results in an elongated to raindrop shape (Cathalot *et al.*, 2015; Corbera *et al.*, 2022). Flume-tank experiments show this may be due to a high particle encounter rate on the up-current side of the structure, after which the flow is deflected over the structure, leaving corals in its wake devoid of food particles (Corbera *et al.*, 2022). This is indeed the case for the mini-mounds in Bilbo and Frodo channels, where the long axis of the mounds is oriented along the orientation of the tidal bottom currents (Figs. 3 and 5).

The same mechanism may lead to self-organisation within cold-water coral colonies and explain the formation of the large coral mound consisting of parallel coral ridges in Bilbo Channel (Fig. 7B,C) (Mienis *et al.*, 2019; Corbera *et al.*, 2022; van der Kaaden *et al.*, 2023). At a certain distance behind one coral structure, the original flow conditions are re-established and a new structure can grow, which could lead to a series of parallel coral patches at regular distances from one another (Corbera *et al.*, 2022). This has been observed on the scale of coral reef fields (Correa *et al.*, 2012), but is here shown on the scale of a single mound. In the case of Bilbo Channel, the higher mound relief on the upslope side, and the higher number of living corals observed there, imply that the downslope-directed current is dominant for the growth of this mound (Messing *et al.*, 1990). From their flume tank experiments, Corbera *et al.* (2022) estimate that flow re-establishment downstream occurs at a distance of 15 to 20 times the height of the coral structure, which fits with the heights (average 0.4 m)

and distances (average 9.8 m) measured on the parallel ridges here. Another hypothesis for the formation of parallel ridges of cold-water corals involves the occupation of ripples or sandwaves by corals (Wheeler *et al.*, 2005; Foubert *et al.*, 2011). However, neither the images nor the bathymetry show any indication of bedforms underneath or surrounding the large coral mound (Fig. 7). Hence, the first hypothesis is preferred. The partly-imaged coral patches to the south and southeast of the large coral mound (Fig. 7A) seemingly form comparable parallel, north–south-oriented structures and may represent a similar but less developed stage of coral mound formation.

Temporal variation in downslope activity

All layers present in core B2306-GC02 and the two grey-coloured layers described in core B2306-GC04 are interpreted as turbidites based on their very fine sand (i.e. coarser than background) lithology, fining-upwards trend in grain size, distinct lower boundaries and distinct to gradual upper boundaries (Figs. 8 and 9). Additionally, their colour differs from the colour of the background sediments, indicating a different sediment source.

For the other layers in core B2306-GC04, the interpretation of the depositional process is more ambiguous. Their limited thicknesses (one to several mm) and dipping geometries make grain size analysis challenging, but where measurable, the layers have a coarser lithology than the background brown muds. The high-resolution grain-size model does not display clear fining-upwards trends within the layers, and no identifiable erosive lower boundaries are present in the CT data. Some of the layers are coloured differently than the background sediments; they show up as either higher or lower intensities in the CT data, and they do not have a consistent signal in the XRF data, implying a sediment source that is different from the background sediments, but not consistent for all layers. Bottom currents are a known process transporting channel floor sediments capable of producing layered deposits (Normandeau *et al.*, 2024). For a large part of the time interval during which the layers were deposited (>22.7 to 16.0 kyr BP: end of Last Glacial Maximum and deglaciation), however, it is thought that bottom currents over the eastern slope of the Porcupine Seabight were too sluggish to transport sand-sized grains exceeding 100 μm (Wienberg *et al.*, 2020). Additionally, core B2306-GC04 is located at a water depth of 1830 m, which—even when accounting for lowered sea levels—is well below the depths where intensified (tidal) bottom currents occur in the basin (c. 700 m) (White, 2007; White *et al.*, 2007). Therefore, although no clear sedimentological arguments can be found to link the layers in core B2306-GC04 to downslope gravity flows, they are thought to be the most likely depositional process producing these layers as well.

These findings imply that downslope gravity flows were active during the Last Glacial Maximum and early deglaciation and reached >35 km down into Bilbo Channel. They remained active until c. 9.6 kyr BP, as implied from the age of the youngest turbidite according to the age model of core B2306-GC02 (Fig. 8). As the gravity flows carried enough sediment to deposit layers of 1 mm – 2 cm thickness at 25 to 35 km along the channel, it was likely not possible for cold-water corals to survive—let alone build up mounded structures—in the upslope channel sections during the time they were active. It is, therefore, proposed that the mini-mounds are younger than 9.6 kyr, which is consistent with other records from the NE Atlantic region (Wienberg & Titschack, 2015). For the corals to build mini-mounds of 2 to 17 m high (7 m average), average aggradation rates of c. 21 to 177 cm kyr^{-1} (73 cm kyr^{-1} average) would be required. This is within the range of aggradation rates calculated for several mounds in the Porcupine Seabight (Frank *et al.*, 2009).

There is no evidence for downslope flows during the c. 6.5 months for which the Bilbo Channel mooring current meter record is reliable. The main indicators for present-day downslope activity are the branched gully systems in the heads of both Bilbo and Frodo channels. In the southernmost branch of the gully system in Frodo Channel, the train of crescentic bedforms (Fig. 4C) along with the presence of the scarps further downslope (Fig. 4D) is indicative of present-day downslope activity (Paull *et al.*, 2010; Normandeau *et al.*, 2014).

Crescentic bedforms with similar shapes, orientations and dimensions located on canyon floors are often interpreted as cyclic steps (Cartigny *et al.*, 2011; Babonneau *et al.*, 2013; Normandeau *et al.*, 2014; Symons *et al.*, 2016; Chen *et al.*, 2021). These upstream-migrating bedforms are the result of hydraulic jumps in downslope flows, where supercritical flow that causes erosion and creates the base of a step, transforms

into subcritical flow that allows deposition at the top of the next step (Kostic *et al.*, 2010). Thus, cyclic steps can be identified based on the presence of hydraulic jumps within downslope flows, or—more commonly, since direct measurements and flow analyses are more challenging than bedform analyses—their upstream-migrating character (Kostic *et al.*, 2010). Here, however, without any flow measurements or information about the internal structure of the described features, it is impossible to confirm their origin as cyclic steps.

Alternatively, if the flows responsible for creating the crescentic bedforms are subcritical, and the bedforms' internal structure shows downstream migration, these features would be interpreted as barchan dunes rather than cyclic steps (Symons *et al.*, 2016; van Dijk *et al.*, 2020). Barchan dunes are generally associated with flow velocities of 0.6 to 1.2 m s^{-1} (Stow *et al.*, 2009), which is within the range of values recorded by direct measurements of downslope gravity flows in submarine canyon-channel systems but lower than the maximum velocity of the most powerful flows (Khripounoff *et al.*, 2012; Azpiroz-Zabala *et al.*, 2017; Paull *et al.*, 2018; Normandeau *et al.*, 2020; Heijnen *et al.*, 2022; Hill & Lintern, 2022; Liu *et al.*, 2023).

Most of the gullies, however, have backscatter characteristics that are not distinguishable from the surrounding seafloor (Fig. 4B). This observation is interpreted as a sign of present-day inactivity and burial of all but one gully by hemipelagic sediments (with a potential bottom-current reworking component). Along with the limited downslope extent of the gully systems, as well as the presence of cold-water coral mounds containing living coral, and the absence of turbidites in the 9.6 to 0 kyr BP record of the two channel floor cores, this indicates that present-day downslope activity is low in volume and frequency. Thus, the GCS can be considered inactive with downslope flows at present.

Due to the spatial limits of the datasets presented here and the lack of data available on the outer Celtic Sea Shelf (Giglio *et al.*, 2021, 2022; Arosio *et al.*, 2023), it is difficult to establish the origin of the downslope flows. Two of the chaotic facies in both cores (299 to 275 cm in core B2306-GC02 and 161 to 152 cm in core B2306-GC04; Figs. 8 and 9) may be interpreted as slump deposits, and slide scars are visible on the channel flanks (Fig. 1; Verweirder *et al.*, 2021), which would point to slope failures of the channel flanks or in the channel heads as potential sources for sediment transport. Another potential source mechanism that could be explored further is channelised systems that were mapped on the inner and mid-shelf and interpreted as conduits for glacial meltwater from the British-Irish Ice Sheet (Giglio *et al.*, 2021, 2022; Arosio *et al.*, 2023). A connection between the meltwater features and the shelf edge has not been established. Lastly, oceanographic processes may create turbidity near the seafloor and promote sediment resuspension, such as near-inertial waves created by wind stress at the ocean surface (e.g. Chinn *et al.*, 2012; Jordi *et al.*, 2016). Further research on outer shelf glacio-marine and oceanographic processes, both in past cold periods and the present-day environment is needed to elucidate on the sediment sources and transport mechanisms responsible for supplying the downslope flows in the Gollum Channel System.

CONCLUSIONS

In this study, bedforms in the upper slope sections of the two northernmost channels in the land-detached Gollum Channel System were analysed to identify which, if any, processes are actively transporting sediment over the channel floors. Tidal bottom currents, possibly intensified by internal waves at the transition between the Eastern North Atlantic Central Water and the underlying Mediterranean Outflow Water, are the main active process and create ripples superimposed on megaripples. Present-day downslope activity is inferred from a train of crescentic bedforms in one of the channel heads. However, the resulting bedforms (gullies, scarps, crescentic bedforms, ripples) have a very limited spatial extent in the upper parts of the channels (<700 m water depth), and therefore, downslope flows are thought to be a low-frequency, low-volume process. Thus, the Gollum Channel System can be considered generally inactive yet dynamic at present.

This contrasts with the channel activity during the Last Glacial Maximum and deglaciation, and into the early Holocene, which was recorded as turbidites in two sediment cores on the channel floor. They indicate that gravity flows extended at least 35 km into the channels to >1830 m water depth from >22.7 to 9.6 cal kyr BP. The present-day combination of the absence of downslope flows and the continuous movement of sediments and food particles

provided by the tidally modulated bottom currents allows the development of cold-water coral mini-mounds on the wide channel floors. The onset of mini-mound growth is thought to coincide with the Holocene inactivity of the Gollum Channel System c. 9.6 cal kyr BP. This demonstrates the importance of (in)activity and bottom current dynamics in canyon-channel systems for deep-sea habitats.

The combination of the very high-resolution AUV data and sediment core records presented here reveals that the Gollum Channel System was active under modern climatic and oceanographic conditions in the early Holocene, after the deglaciation of the continental shelf and the detachment of the system from terrestrial sources. The processes that allowed this early Holocene activity are yet unknown. Nevertheless, this finding further challenges the idea that submarine canyon-channel systems are inactive during periods of high sea levels. The contrast between the Gollum Channel System (currently inactive) and the Whittard Canyon (currently active), situated less than 200 km apart and draining the same continental shelf, indicates that although land-detached canyon-channel systems can indeed experience frequent present-day activity, specific environmental controls are required and should be investigated for each individual system.

ACKNOWLEDGEMENTS

Author LV is funded by the Research Foundation-Flanders (FWO grant 1114521N) and the Special Research Fund (BOF) of Ghent University. XRF analyses were partly funded by a Postgraduate Research Grant from the International Association of Sedimentologists. This manuscript contains Irish Public Sector Data (Geological Survey Ireland & Marine Institute) licensed under a Creative Commons Attribution 4.0 International (CC BY 4.0) licence. We would like to thank the captains and crews of the Irish and UK research vessels for assisting with the collection of the INFOMAR datasets, as well as the captains and crews of RV Celtic Explorer campaign CE21015 and RV Belgica campaigns 2022-18 and 2023-12. We are grateful to A. Ramisch, H. Braun and L. Schley at the Austrian Core Scanning Facility of the University of Innsbruck for their help with XRF core scanning. A. Matossian and P. Reyniers are thanked for constructive discussions that helped improve this manuscript. We are grateful to K. Verweirder for his help with compiling the AUV images into video clips. The authors wish to thank the four reviewers for their feedback that improved this manuscript.

CONFLICT OF INTEREST

The authors declare that they have no known conflicts of interest.

DATA AVAILABILITY STATEMENT

INFOMAR data are available from the INFOMAR Marine Data Download Portal at https://www.infomar.ie/data (Geological Survey Ireland & Marine Institute, 2024). The RV Celtic Explorer and RV Belgica bathymetry data, sediment core data and AUV data of this study are available from the corresponding author upon reasonable request.

REFERENCES

Antsey, K.J., **Klymak, J.M.**, **Mihaly, S.F.** and **Thomson, R.E.** (2024) Internal waves force elevated turbulent mixing at Barkley canyon. *J. Geophys. Res. Oceans*, **219**, e2023JC020760.

Arosio, R., **Wheeler, A.J.**, **Sacchetti, F.**, **Guinan, J.**, **Benetti, S.**, **O'Keefe, E.**, **van Landeghem, K.J.J.**, **Conti, L.A.**, **Furey, T.** and **Lim, A.** (2023) The geomorphology of Ireland's continental shelf. *J. Maps*, **19**, 1–26.

Aslam, T., **Hall, R.A.** and **Dye, S.R.** (2018) Internal tides in a dendritic submarine canyon. *Prog. Oceanogr.*, **169**, 20–32.

Azpiroz-Zabala, M., **Cartigny, M.J.B.**, **Talling, P.J.**, **Parsons, D.R.**, **Sumner, E.J.**, **Clare, M.A.**, **Simmons, S.M.**, **Cooper, C.** and **Pope, E.L.** (2017) Newly recognized turbidity current structure can explain prolonged flushing of submarine canyons. *Sci. Adv.*, **3**, e1700200.

Babonneau, N., **Delacourt, C.**, **Cancouët, R.**, **Sisavath, E.**, **Bachèlery, P.**, **Mazuel, A.**, **Jorry, S.J.**, **Deschamps, A.**, **Ammann, J.** and **Villeneuve, N.** (2013) Direct sediment transfer from land to deep-sea: insights into shallow multibeam bathymetry at La Réunion Island. *Mar. Geol.*, **346**, 47–57.

Baker, M.L., **Hage, S.**, **Talling, P.J.**, **Acikalin, S.**, **Hilton, R.G.**, **Haghipour, N.**, **Ruffell, S.C.**, **Pope, E.L.**, **Jacinto, R.S.**, **Clare, M.A.** and **Sahin, S.** (2024) Globally significant mass of terrestrial organic carbon efficiently transported by canyon-flushing turbidity currents. *Geology*, **52**, 631–636.

Bernhardt, A. and **Schwanghart, W.** (2021) Where and why do submarine canyons remain connected to the shore during sea-level rise? Insights from global topographic analysis and Bayesian regression. *Geophys. Res. Lett.*, **48**, e2020GL092234.

Bernhardt, A., **Melnick, D.**, **Jara-Muñoz, J.**, **Argandoña, B.**, **González, J.** and **Strecker, M.R.** (2015) Controls on

submarine canyon activity during sea-level highstands: the Biobío canyon system offshore Chile. *Geosphere*, **11**, 1226–1255.

Bertrand, S., **Tjallingii, R.**, **Kylander, M.E.**, **Wilhelm, B.**, **Roberts, S.J.**, **Arnaud, F.**, **Brown, E.** and **Bindler, R.** (2024) Inorganic geochemistry of lake sediments: a review of analytical techniques and guidelines for data interpretation. *Earth Sci. Rev.*, **249**, 104639.

Blaauw, M. and **Christen, J.A.** (2011) Flexible paleoclimate age-depth models using an autoregressive gamma process. *Bayesian Anal.*, **6**, 457–474.

Bourillet, J.F., **Zaragosi, S.** and **Mulder, T.** (2006) The French Atlantic margin and deep-sea submarine systems. *Geo-Mar. Lett.*, **26**, 311–315.

Brooke, S. and **Ross, S.W.** (2014) First observations of the cold-water coral *Lophelia pertusa* in mid-Atlantic canyons of the USA. *Deep Sea Res. Part II Top. Stud. Oceanogr.*, **104**, 245–251.

Canals, M., **Puig, P.**, **de Durrieu Madron, X.**, **Heussner, S.**, **Palanques, A.** and **Fabres, J.** (2006) Flushing submarine canyons. *Nature*, **444**, 354–357.

Cartigny, M.J.B., **Postma, G.**, **van den Berg, J.H.** and **Mastbergen, D.R.** (2011) A comparative study of sediment waves and cyclic steps based on geometries, internal structures and numerical modeling. *Mar. Geol.*, **280**, 40–56.

Cataño-Lopera, Y.A. and **García, M.H.** (2006) Geometry and migration characteristics of bedforms under waves and currents. Part 1: Sandwave morphodynamics. *Coast. Eng.*, **53**, 767–780.

Cathalot, C., **Van Oevelen, D.**, **Cox, T.J.S.**, **Kutti, T.**, **Lavaleye, M.**, **Duineveld, G.** and **Meysman, F.J.R.** (2015) Cold-water coral reefs and adjacent sponge grounds: hotspots of benthic respiration and organic carbon cycling in the deep sea. *Front. Mar. Sci.*, **2**, 37.

Chen, Y., **Parsons, D.R.**, **Simmons, S.M.**, **Williams, R.**, **Cartigny, M.J.B.**, **Hughes Clarke, J.E.**, **Stacey, C.D.**, **Hage, S.**, **Talling, P.J.**, **Azpiroz-Zabala, M.**, **Clare, M.A.**, **Hizzett, J.L.**, **Heijnen, M.S.**, **Hunt, J.E.**, **Lintern, D.G.**, **Sumner, E.J.**, **Vellinga, A.J.** and **Vendettuoli, D.** (2021) Knickpoints and crescentic bedform interactions in submarine channels. *Sedimentology*, **68**, 1358–1377.

Chinn, B.S., **Girton, J.B.** and **Alford, M.H.** (2012) Observations of internal waves and parametric subharmonic instability in the Philippines archipelago. *J. Geophys. Res.*, **117**, C05019.

Clark, C.D., **Ely, J.C.**, **Fabel, D.** and **Bradley, S.L.** (2022a) BRITICE-CHRONO maps and GIS data of the last British-Irish Ice Sheet 31 to 15 ka, including model reconstruction, geochronometric age spreadsheet, palaeotopographies and coastline positions [dataset]. PANGAEA. https://doi.org/10.1594/PANGAEA.945729.

Clark, C.D., **Ely, J.C.**, **Hindmarsh, R.C.A.**, **Bradley, S.**, **Ignéczi, A.**, **Fabel, D.**, **Ó Cofaigh, C.**, **Chiverrell, R.C.**, **Scourse, J.**, **Benetti, S.**, **Bradwell, T.**, **Evans, D.J.A.**, **Roberts, D.H.**, **Burke, M.**, **Callard, S.L.**, **Medialdea, A.**, **Saher, M.**, **Small, D.**, **Smedley, R.K.**, **Gasson, E.**, **Gregoire, L.**, **Gandy, N.**, **Hughes, A.L.C.**, **Ballantyne, C.**, **Bateman, M.D.**, **Bigg, G.R.**, **Doole, J.**, **Dove, D.**, **Duller, G.A.T.**, **Jenkins, G.T.H.**, **Livingstone, S.L.**, **McCarron, S.**, **Moreton, S.**, **Pollard, D.**, **Praeg, D.**, **Sejrup, H.P.**, **Van Landeghem, K.J.J.** and **Wilson, P.** (2022b) Growth and retreat of the last British–Irish Ice Sheet, 31 000 to 15 000 years ago: the BRITICE-CHRONO reconstruction. *Boreas*, **51**, 699–758.

Collart, T., **Verreydt, W.**, **Hernández-Molina, F.J.**, **Llave, E.**, **León, R.**, **Gómez-Ballesteros, M.**, **Pons-Branchu, E.**, **Stewart, H.** and **Van Rooij, D.** (2018) Sedimentary processes and cold-water coral mini-mounds at the Ferrol canyon head, NW Iberian margin. *Prog. Oceanogr.*, **169**, 48–65.

Corbera, G., **Lo Iacono, C.**, **Simarro, G.**, **Grinyó, J.**, **Ambroso, S.**, **Huvenne, V.A.I.**, **Mienis, F.**, **Carreiro-Silva, M.**, **Martins, I.**, **Mano, B.**, **Orejas, C.**, **Larsson, A.**, **Hennige, S.** and **Gori, A.** (2022) Local-scale feedbacks influencing cold-water coral growth and subsequent reef formation. *Sci. Rep.*, **12**, 20389.

Correa, T.B.S., **Eberli, G.P.**, **Grasmueck, M.**, **Reed, J.K.** and **Correa, A.M.S.** (2012) Genesis and morphology of cold-water coral ridges in a unidirectional current regime. *Mar. Geol.*, **326–328**, 14–27.

Covault, J.A. and **Graham, S.A.** (2010) Submarine fans at all sea-level stands: tectono-morphologic and climatic controls on terrigenous sediment delivery to the deep sea. *Geology*, **38**, 939–942.

Daly, E., **Johnson, M.P.**, **Wilson, A.M.**, **Gerritsen, H.D.**, **Kiriakoulakis, K.**, **Allcock, A.L.** and **White, M.** (2018) Bottom trawling at Whittard Canyon: evidence for seabed modification, trawl plumes and food source heterogeneity. *Prog. Oceanogr.*, **169**, 227–240.

De Clippele, L.H., **Gafeira, J.**, **Robert, K.**, **Hennige, S.**, **Lavaleye, M.S.**, **Duineveld, G.C.A.**, **Huvenne, V.A.I.** and **Roberts, J.M.** (2017) Using novel acoustic and visual mapping tools to predict the small-scale spatial distribution of live biogenic reef framework in cold-water coral habitats. *Coral Reefs*, **36**, 255–268.

De Mol, L., **Van Rooij, D.**, **Pirlet, H.**, **Greinert, J.**, **Frank, N.**, **Quemmerais, F.** and **Henriet, J.-P.** (2011) Cold-water coral habitats in the Penmarc'h and Guilvinec Canyons (Bay of Biscay): deep-water versus shallow-water settings. *Mar. Geol.*, **282**, 40–52.

van Dijk, T.A.G.P., **Best, J.** and **Baas, A.C.W.** (2020) Subaqueous and subaerial depositional bedforms. In: *Encyclopedia of Geology: Volume 1-6*, Vol. **2**, 2nd edn, pp. 771–786. Elsevier.

Duineveld, G.C.A., **Lavaleye, M.S.S.**, **Bergman, M.J.N.**, **De Stigter, H.** and **Mienis, F.** (2007) Trophic structure of a cold-water coral mound community (Rockall Bank, NE Atlantic) in relation to the near-bottom particle supply and current regime. *Bull. Mar. Sci.*, **81**, 449–467.

Dullo, W.-C., **Flögel, S.** and **Rüggeberg, A.** (2008) Cold-water coral growth in relation to the hydrography of the Celtic and Nordic European continental margin. *Mar. Ecol. Prog. Ser.*, **371**, 165–176.

Foubert, A., **Huvenne, V.A.I.**, **Wheeler, A.**, **Kozachenko, M.**, **Opderbecke, J.** and **Henriet, J.P.** (2011) The Moira Mounds, small cold-water coral mounds in the Porcupine Seabight, NE Atlantic: part B-evaluating the impact of sediment dynamics through high-resolution ROV-borne bathymetric mapping. *Mar. Geol.*, **282**, 65–78.

Frank, N., **Ricard, E.**, **Lutringer-Paquet, A.**, **van der Land, C.**, **Colin, C.**, **Blamart, D.**, **Foubert, A.**, **Van Rooij, D.**, **Henriet, J.-P.**, **de Haas, H.** and **van Weering, T.** (2009) The Holocene occurrence of cold water corals in the NE Atlantic: implications for coral carbonate mound evolution. *Mar. Geol.*, **266**, 129–142.

Freiwald, A., **Fossså, J.H.**, **Grehan, A.**, **Koslow, T.** and **Roberts, J.M.** (2004) *Cold-Water Coral Reefs: Out of Sight – No Longer Out of Mind*. UNEP-WCMC, Cambridge, UK.

GEBCO Compilation Group. (2023) GEBCO 2023 Grid. Available at: https://www.gebco.net/.

Geological Survey Ireland and Marine Institute. (2024) Infomar. Available at: https://www.infomar.ie/data.

Giglio, C., **Benetti, S.**, **Sacchetti, F.**, **Lockhart, E.**, **Hughes Clarke, J.**, **Plets, R.**, **Van Landeghem, K.**, **Ó Cofaigh, C.**, **Scourse, J.** and **Dunlop, P.** (2021) A Late Pleistocene channelized subglacial meltwater system on the Atlantic continental shelf south of Ireland. *Boreas*, **51**, 118–135.

Giglio, C., **Benetti, S.**, **Plets, R.M.K.**, **Dunlop, P.**, **Ó Cofaigh, C.**, **Sacchetti, F.** and **Salomon, E.** (2022) Character of advance and tretreat of the southwest sector of the British-Irish Ice Sheet during the last glaciation. *Quat. Sci. Rev.*, **291**, 107655.

Glogowski, S., **Dullo, W.-C.**, **Feldens, P.**, **Liebetrau, V.**, **von Reumont, J.**, **Hühnerbach, V.**, **Krastel, S.**, **Wynn, R.B.** and **Flögel, S.** (2015) The Eugen Seibold coral mounds offshore western Morocco: oceanographic and bathymetric boundary conditions of a newly discovered cold-water coral province. *Geo-Mar. Lett.*, **35**, 257–269.

Guerrero, Q. and **Guillén, J.** (2020) Dynamics of ripples superimposed on a sand ridge on a tideless shoreface. *Estuar. Coast. Shelf Sci.*, **242**, 106826.

Harris, P.T. and **Whiteway, T.** (2011) Global distribution of large submarine canyons: geomorphic differences between active and passive continental margins. *Mar. Geol.*, **285**, 69–86.

Harris, P.T., **Macmillan-Lawler, M.**, **Rupp, J.** and **Baker, E.K.** (2014) Geomorphology of the oceans. *Mar. Geol.*, **352**, 4–24.

Heaton, T.J., **Köhler, P.**, **Butzin, M.**, **Bard, E.**, **Reimer, R.W.**, **Austin, W.E.N.**, **Bronk Ramsey, C.**, **Grootes, P.M.**, **Hughen, K.A.**, **Kromer, B.**, **Reimer, P.J.**, **Adkins, J.**, **Burke, A.**, **Cook, M.S.**, **Olsen, J.** and **Skinner, L.C.** (2020) Marine20—the marine radiocarbon age calibration curve (0–55,000 cal BP). *Radiocarbon*, **62**, 779–820.

Hebbeln, D., **Wienberg, C.**, **Wintersteller, P.**, **Freiwald, A.**, **Becker, M.**, **Beuck, L.**, **Dullo, C.**, **Eberli, G.P.**, **Glogowski, S.**, **Matos, L.**, **Forster, N.**, **Reyes-Bonilla, H.**, **Taviani, M.** and **MSM 20–4 shipboard scientific party** (2014) Environmental forcing of the Campeche cold-water coral province, southern Gulf of Mexico. *Biogeosciences*, **11**, 1799–1815.

Heijnen, M.S., **Mienis, F.**, **Gates, A.R.**, **Bett, B.J.**, **Hall, R.A.**, **Hunt, J.**, **Kane, I.A.**, **Pebody, C.**, **Huvenne, V.A.I.**, **Soutter, E.L.** and **Clare, M.A.** (2022) Challenging the highstand-dormant paradigm for land-detached submarine canyons. *Nat. Commun.*, **13**, 1–11.

Hennige, S.J., **Larsson, A.I.**, **Orejas, C.**, **Gori, A.**, **De Clippele, L.H.**, **Lee, Y.C.**, **Jimeno, G.**, **Georgoulas, K.**, **Kamenos, N.A.** and **Roberts, J.M.** (2021) Using the Goldilocks principle to model coral ecosystem engineering. *Proc. R. Soc. B Biol. Sci.*, **288**, 20211260.

Herbert, C.M., **Alexander, J.** and **de Álvaro, M.J.M.** (2015) Back-flow ripples in troughs downstream of unit bars: formation, preservation and value for interpreting flow conditions. *Sedimentology*, **62**, 1814–1836.

Hill, P.R. and **Lintern, D.G.** (2022) Turbidity currents on the open slope of the Fraser Delta. *Mar. Geol.*, **445**, 106738.

Hsu, S.K., **Kuo, J.**, **Lo, C.L.**, **Tsai, C.H.**, **Doo, W.B.**, **Ku, C.Y.** and **Sibuet, J.C.** (2008) Turbidity currents, submarine landslides and the 2006 Pingtung Earthquake off SW Taiwan. *Terr. Atmos. Ocean. Sci.*, **19**, 767–772.

Huvenne, V.A.I., **Beyer, A.**, **de Haas, H.**, **Dekindt, K.**, **Henriet, J.-P.**, **Kozachenko, M.**, **Olu-Le Roy, K.** and **Wheeler, A.J.** (2005) The seabed appearance of different coral bank provinces in the Porcupine Seabight, NE Atlantic: results from sidescan sonar and ROV seabed mapping. In: *Cold-Water Corals and Ecosystems* (Eds Freiwald, A. and Roberts, J.M.), pp. 535–569. Springer, Berlin, Heidelberg.

Huvenne, V.A.I., **Masson, D.G.** and **Wheeler, A.J.** (2009a) Sediment dynamics of a sandy contourite: the sedimentary context of the Darwin cold-water coral mounds, Northern Rockall Trough. *Int. J. Earth Sci.*, **98**, 865–884.

Huvenne, V.A.I., **Van Rooij, D.**, **De Mol, B.**, **Thierens, M.**, **O'Donnell, R.** and **Foubert, A.** (2009b) Sediment dynamics and palaeo-environmental context at key stages in the challenger cold-water coral mound formation: clues from sediment deposits at the mound base. *Deep Sea Res. Part I Oceanogr. Res. Pap.*, **56**, 2263–2280.

Huvenne, V.A.I., **Tyler, P.A.**, **Masson, D.G.**, **Fisher, E.H.**, **Hauton, C.**, **Hühnerbach, V.**, **Le Bas, T.P.** and **Wolff, G.A.** (2011) A picture on the wall: innovative mapping reveals cold-water coral refuge in submarine canyon. *PLoS One*, **6**, e28755.

Jaijel, R., **Biton, E.**, **Weinstein, Y.**, **Ozer, T.** and **Katz, T.** (2023) Observations of turbidity currents in a small, slope-confined submarine canyon in the Eastern Mediterranean Sea. *Earth Planet. Sci. Lett.*, **604**, 118008.

Jordi, A., **Dong-Ping, W.** and **Hamilton, P.** (2016) Near-inertial motions in the DeSoto Canyon during Hurricane Georges. *Ocean Model*, **105**, 34–43.

van der Kaaden, A.-S., **Maier, S.R.**, **Siteur, K.**, **De Clippele, L.H.**, **van de Koppel, J.**, **Purkis, S.J.**, **Rietkerk, M.**, **Soetaert, K.** and **van Oevelen, D.** (2023) Tiger reefs: Self-organized regular patterns in deep-sea cold-water coral reefs. *Ecosphere*, **14**, e4654.

Kane, I.A. and **Clare, M.A.** (2019) Dispersion, accumulation, and the ultimate fate of microplastics in deep-marine environments: a review and future directions. *Front. Earth Sci.*, **7**, 80.

Khripounoff, A., **Crassous, P.**, **Lo Bue, N.**, **Dennielou, B.** and **Silva Jacinto, R.** (2012) Different types of sediment gravity flows detected in the Var submarine canyon (northwestern Mediterranean Sea). *Prog. Oceanogr.*, **106**, 138–153.

Kostic, S., **Sequeiros, O.**, **Spinewine, B.** and **Parker, G.** (2010) Cyclic steps: a phenomenon of supercritical shallow flow from the high mountains to the bottom of the ocean. *J. Hydro-Environ. Res.*, **3**, 167–172.

Kwoll, E., **Venditti, J.G.**, **Bradley, R.W.** and **Winter, C.** (2016) Flow structure and resistance over subaquaeous high- and low-angle dunes. *Case Rep. Med.*, **121**, 545–564.

Li, M.Z. and **King, E.L.** (2007) Multibeam bathymetric investigations of the morphology of sand ridges and associated bedforms and their relation to storm processes, Sable Island Bank, Scotian Shelf. *Mar. Geol.*, **243**, 200–228.

Li, Y., **Clift, P.D.**, **Böning, P.**, **Blusztajn, J.**, **Murray, R.W.**, **Ireland, T.**, **Pahnke, K.**, **Helm, N.C.** and **Giosan, L.** (2018) Continuous Holocene input of river sediment to the Indus Submarine Canyon. *Mar. Geol.*, **406**, 159–176.

Liu, D., **Bertrand, S.** and **Weltje, G.J.** (2019) An empirical method to predict sediment grain size from inorganic geochemical measurements. *Geochem. Geophys. Geosyst.*, **20**, 3690–3704.

Liu, M., **Wang, Z.**, **Yu, K.** and **Xu, J.** (2023) Two distinct types of turbidity currents observed in the Manila Trench, South China Sea. *Commun. Earth Environ.*, **4**, 108.

Lo Iacono, C., **Guillén, J.**, **Guerrero, Q.**, **Durán, R.**, **Wardell, C.**, **Hall, R.A.**, **Aslam, T.**, **Carter, G.D.O.**, **Gales, J.A.** and **Huvenne, V.A.I.** (2020) Bidirectional bedform fields at the head of a submarine canyon (NE Atlantic). *Earth Planet. Sci. Lett.*, **542**, 116321.

Maier, K.L., **Rosenberger, K.J.**, **Paull, C.K.**, **Gwiazda, R.**, **Gales, J.**, **Lorenson, T.**, **Barry, J.P.**, **Talling, P.J.**, **McGann, M.**, **Xu, J.**, **Lundsten, E.**, **Anderson, K.**, **Litvin, S.Y.**, **Parsons, D.R.**, **Clare, M.A.**, **Simmons, S.M.**, **Sumner, E.J.** and **Cartigny, M.J.B.** (2019) Sediment and organic carbon transport and deposition driven by internal tides along Monterey Canyon, offshore California. *Deep Sea Res. Part I Oceanogr. Res. Pap.*, **153**, 103108.

Masson, D.G., **Bett, B.J.**, **Billett, D.S.M.**, **Jacobs, C.L.**, **Wheeler, A.J.** and **Wynn, R.B.** (2003) The origin of deep-water coral-topped mounds in the northern Rockall Trough, Northeast Atlantic. *Mar. Geol.*, **194**, 159–180.

Matossian, A.O. and **Van Rooij, D.** (2024) Morphosedimentary evolution of the Belgica Mound Drift: controls on contourite depositional system development in association with cold-water coral mounds. *Mar. Geol.*, **477**, 107410.

McDonnell, A. and **Shannon, P.M.** (2001) Comparative Tertiary stratigraphic evolution of the Porcupine and Rockall basins. *Geol. Soc. Lond. Spec. Publ.*, **188**, 323–344.

Messing, C.G., **Neumann, A.C.** and **Lang, J.C.** (1990) Biozonation of Deep-Water Lithoherms and Associated Hardgrounds in the Northeastern Straits of Florida. *Palaios*, **5**, 15–33.

Mevik, B.-H. and **Wehrens, R.** (2007) The pls package: principal component and partial least squares regression in R. *J. Stat. Softw.*, **18**, 1–23.

Mienis, F., **Bouma, T.J.**, **Witbaard, R.**, **van Oevelen, D.** and **Duineveld, G.C.A.** (2019) Experimental assessment of the effects of cold-water coral patches on water flow. *Mar. Ecol. Prog. Ser.*, **609**, 101–117.

Morris, K.J., **Tyler, P.A.**, **Masson, D.G.**, **Huvenne, V.A.I.** and **Rogers, A.D.** (2013) Distribution of cold-water corals in the Whittard Canyon, NE Atlantic Ocean. *Deep Sea Res. II Top. Stud. Oceanogr.*, **92**, 136–144.

Mortensen, P.B. and **Buhl-Mortensen, L.** (2005) Deep-water corals and their habitats in the gully, a submarine canyon off Atlantic Canada. In: *Cold-Water Corals and Ecosystems* (Eds Freiwald, A. and Roberts, J.M.), pp. 247–277. Springer-Verlag, Berlin, Heidelberg.

Mountjoy, J.J., **Micallef, A.**, **Stevens, C.L.** and **Stirling, M.W.** (2014) Holocene sedimentary activity in a non-terrestrially coupled submarine canyon: Cook Strait Canyon system, New Zealand. *Deep Sea Res. II Top. Stud. Oceanogr.*, **104**, 120–133.

Mulder, T., **Zaragosi, S.**, **Garlan, T.**, **Mavel, J.**, **Cremer, M.**, **Sottolichio, A.**, **Sénéchal, N.** and **Schmidt, S.** (2012) Present deep-submarine canyons activity in the Bay of Biscay (NE Atlantic). *Mar. Geol.*, **295–298**, 113–127.

Naqshband, S., **Ribberink, J.S.**, **Hurther, D.** and **Hulscher, S.J.M.H.** (2014) Bed load and suspended load contributions to migrating sand dunes in equilibrium. *Case Rep. Med.*, **119**, 1043–1063.

Naylor, D. and **Shannon, P.M.** (2005) The structural framework of the Irish Atlantic Margin. In: *Petroleum Geology: North-West Europe and Global Perspectives - Proceedings of the 6th Petroleum Geology Conference* (Eds Doré, A.G. and Vining, B.A.), Vol. **6**, pp. 1009–1021. Geological Society, London.

Normandeau, A., **Lajeunesse, P.**, **St-Onge, G.**, **Bourgault, D.**, **Drouin, S.S.-O.**, **Senneville, S.** and **Bélanger, S.** (2014) Morphodynamics in sediment-starved inner-shelf submarine canyons (Lower St. Lawrence Estuary, Eastern Canada). *Mar. Geol.*, **357**, 243–255.

Normandeau, A., **Bourgault, D.**, **Neumeier, U.**, **Lajeunesse, P.**, **St-Onge, G.**, **Gostiaux, L.** and **Chavanne, C.** (2020) Storm-induced turbidity currents on a sediment-starved shelf: insight from direct monitoring and repeat seabed mapping of upslope migrating bedforms. *Sedimentology*, **67**, 1045–1068.

Normandeau, A., **Dafoe, L.T.**, **Li, M.Z.**, **Campbell, D.C.** and **Jenner, K.A.** (2024) Sedimentary record of bottom currents and internal tides in a modern highstand submarine canyon head. *Sedimentology*, **71**, 1061–1083.

Orejas, C., **Gori, A.**, **Lo Iacono, C.**, **Puig, P.**, **Gili, J.-M.** and **Dale, M.R.T.** (2009) Cold-water corals in the Cap de Creus canyon, northwestern Mediterranean: spatial distribution, density and anthropogenic impact. *Mar. Ecol. Prog. Ser.*, **397**, 37–51.

Passchier, S. and **Kleinhans, M.G.** (2005) Observations of sand waves, megaripples, and hummocks in the Dutch coastal area and their relation to currents and combined flow conditions. *Case Rep. Med.*, **110**, F04S15.

Paull, C.K., **Ussler, W.**, **Caress, D.W.**, **Lundsten, E.**, **Covault, J.A.**, **Maier, K.L.**, **Xu, J.** and **Augenstein, S.** (2010) Origins of large crescent-shaped bedforms within the axial channel of Monterey Canyon, Offshore California. *Geosphere*, **6**, 755–774.

Paull, C.K., **Talling, P.J.**, **Maier, K.L.**, **Parsons, D.**, **Xu, J.**, **Caress, D.W.**, **Gwiazda, R.**, **Lundsten, E.M.**, **Anderson, K.**, **Barry, J.P.**, **Chaffey, M.**, **O'Reilly, T.**, **Rosenberger, K.J.**, **Gales, J.A.**, **Kieft, B.**, **McGann, M.**, **Simmons, S.M.**, **McCann, M.**, **Sumner, E.J.**, **Clare, M.A.** and **Cartigny, M.J.** (2018) Powerful turbidity currents driven by dense basal layers. *Nat. Commun.*, **9**, 4114.

Pierdomenico, M., **Bernhardt, A.**, **Eggenhuisen, J.T.**, **Clare, M.A.**, **Lo Iacono, C.**, **Casalbore, D.**, **Davies, J.S.**, **Kane, I.**, **Huvenne, V.A.I.** and **Harris, P.T.** (2023) Transport and accumulation of litter in submarine canyons: a geoscience perspective. *Front. Mar. Sci.*, **10**, 1224859.

Pingree, R.D. and **Le Cann, B.** (1990) Structure, strength and seasonality of the slope currents in the Bay of Biscay region. *J. Mar. Biol. Assoc. U. K.*, **70**, 857–885.

Praeg, D., **Stoker, M.S.**, **Shannon, P.M.**, **Ceramicola, S.**, **Hjelstuen, B.**, **Laberg, J.S.** and **Mathiesen, A.** (2005) Episodic Cenozoic tectonism and the development of the NW European "passive" continental margin. *Mar. Pet. Geol.*, **22**, 1007–1030.

Puig, P., **Ogston, A.S.**, **Mullenbach, B.L.**, **Nittrouer, C.A.**, **Parsons, J.D.** and **Sternberg, R.W.** (2004) Storm-induced sediment gravity flows at the head of the Eel submarine canyon, northern California margin. *J. Geophys. Res.*, **109**, C03019.

Puig, P., **Palanques, A.** and **Martín, J.** (2014) Contemporary sediment-transport processes in submarine canyons. *Annu. Rev. Mar. Sci.*, **6**, 53–77.

Quan, X. and **Fry, E.S.** (1995) Empirical equation for the index of refraction of seawater. *Appl. Opt.*, **34**, 3477–3480.

Reesink, A.J.H. and **Bridge, J.S.** (2007) Influence of superimposed bedforms and flow unsteadiness on formation of cross strata in dunes and unit bars. *Sediment. Geol.*, **202**, 281–296.

Reesink, A.J.H. and **Bridge, J.S.** (2009) Influence of bedform superimposition and flow unsteadiness on the formation of cross strata in dunes and unit bars – Part 2, further experiments. *Sed. Geol.*, **222**, 274–300.

Rice, A.L., **Billett, D.S.M.**, **Thurston, M.H.** and **Lampitt, R.S.** (1991) The Institute of Oceanographic Sciences Biology Programme in the Porcupine Seabight: background and general introduction. *J. Mar. Biol. Assoc. U. K.*, **71**, 281–310.

Roberts, J.M., **Wheeler, A.J.** and **Freiwald, A.** (2006) Reefs of the deep: the biology and geology of cold-water coral ecosystems. *Science (1979)*, **312**, 543–547.

Sánchez, F., **González-Pola, C.**, **Druet, M.**, **García-Alegre, A.**, **Acosta, J.**, **Cristobo, J.**, **Parra, S.**, **Ríos, P.**, **Altuna, Á.**, **Gómez-Ballesteros, M.**, **Muñoz-Recio, A.**, **Rivera, J.** and **Guillermo, D.d.R.** (2014) Habitat characterization of deep-water coral reefs in La Gaviera Canyon (Avilés Canyon System, Cantabrian Sea). *Deep Sea Res. II Top. Stud. Oceanogr.*, **106**, 118–140.

Scourse, J.D., **Chiverrell, R.c.**, **Smedley, R.K.**, **Small, D.**, **Burke, M.J.**, **Saher, M.**, **Van Landeghem, K.J.J.**, **Duller, G.A.T.**, **Ó Cofaigh, C.**, **Bateman, M.D.**, **Benetti, S.**, **Bradley, S.**, **Callard, L.**, **Evans, D.J.A.**, **Fabel, D.**, **Jenkins, G.T.H.**, **Mc Carron, S.**, **Medialdea, A.**, **Moreton, S.**, **Ou, X.**, **Praeg, D.**, **Roberts, D.H.**, **Roberts, H.M.** and **Clark, C.D.** (2021) Maximum extent and readvance dynamics of the Irish Sea Ice Stream and Irish Sea Glacier since the Last Glacial. *J. Quatern. Sci.*, **36**, 780–804.

Shannon, P.M. (1991) The development of Irish offshore sedimentary basins. *J. Geol. Soc. Lond.*, **148**, 181–189.

Shannon, P.M., **McDonnell, A.** and **Bailey, W.R.** (2007) The evolution of the Porcupine and Rockall basins, offshore Ireland: the geological template for carbonate mound development. *Int. J. Earth Sci.*, **96**, 21–35.

Somoza, L., **Ercilla, G.**, **Urgorri, V.**, **León, R.**, **Medialdea, T.**, **Paredes, M.**, **Gonzalez, F.J.** and **Nombela, M.A.** (2014) Detection and mapping of cold-water coral mounds and living Lophelia reefs in the Galicia Bank, Atlantic NW Iberia margin. *Mar. Geol.*, **349**, 73–90.

Stewart, H.A., **Davies, J.S.**, **Guinan, J.** and **Howell, K.L.** (2014) The Dangeard and Explorer canyons, South Western Approaches UK: geology, sedimentology and newly discovered cold-water coral mini-mounds. *Deep-Sea Res. II Top. Stud. Oceanogr.*, **104**, 230–244.

Stoker, M.S., **Praeg, D.**, **Shannon, P.M.**, **Hjelstuen, B.O.**, **Laberg, J.S.**, **Nielsen, T.**, **van Weering, T.C.E.**, **Sejrup, H.P.** and **Evans, D.** (2005) Neogene evolution of the Atlantic continental margin of NW Europe (Lofoten Islands to SW Ireland): Anything but passive. *Petrol. Geol. Conf. Proc.*, **6**, 1057–1076.

Stow, D.A.V., **Hernández-Molina, F.J.**, **Llave, E.**, **Sayago-Gil, M.**, **del Díaz- Río, V.** and **Branson, A.** (2009) Bedform-velocity matrix: the estimation of bottom current velocity from bedform observations. *Geology*, **37**, 327–330.

Symons, W.O., **Sumner, E.J.**, **Talling, P.J.**, **Cartigny, M.J.B.** and **Clare, M.A.** (2016) Large-scale sediment waves and scours on the modern seafloor and their implications for the prevalence of supercritical flows. *Mar. Geol.*, **371**, 130–148.

Tudhope, A.W. and **Scoffin, T.P.** (1995) Processes of sedimentation in Gollum Channel, Porcupine Seabight: submersible observations and sediment analyses. *Trans. R. Soc. Edinb. Earth Sci.*, **86**, 49–55.

Tyler, P., **Amaro, T.**, **Arzola, R.**, **Cunha, M.R.**, **De Stigter, H.**, **Gooday, A.**, **Huvenne, V.**, **Ingels, J.**, **Kiriakoulakis, K.**, **Lastras, G.**, **Masson, D.**, **Oliveira, A.**, **Pattenden, A.**, **Vanreusel, A.**, **Van Weering, T.**, **Vitorino, J.**, **Witte, U.** and **Wolff, G.** (2009) Europe's Grand Canyon Nazaré Submarine Canyon. *Oceanography*, **22**, 46–57.

Van Rooij, D., **Blamart, D.**, **Kozachenko, M.** and **Henriet, J.-P.** (2007) Small mounded contourite drifts associated with deep-water coral banks, Porcupine Seabight, NE Atlantic Ocean. *Geol. Soc. London Spec. Publ.*, **276**, 225–244.

Venditti, J.G., **Church, M.** and **Bennett, S.J.** (2005) Morphodynamics of small-scale superimposed sand waves over migrating dune bed forms. *Water Resour. Res.*, **41**, W10423.

Verweirder, L., **Van Rooij, D.**, **White, M.**, **Van Landeghem, K.**, **Bossée, K.** and **Georgiopoulou, A.** (2021) Combined control of bottom and turbidity currents on the origin and evolution of channel systems, examples from the Porcupine Seabight. *Mar. Geol.*, **442**, 106639.

Verweirder, L., **Van Rooij, D.** and **Georgiopoulou, A.** (2023) Margin processes sculpting a land-detached canyon-channel system: the Gollum Channel System in the Porcupine Seabight. *Front. Earth Sci.*, **11**, 1285171. https://doi.org/10.3389/feart.2023.1285171.

Wheeler, A.J., **Kenyon, N.H.**, **Ivanov, M.K.**, **Beyer, A.**, **Cronin, B.T.**, **McDonnell, A.**, **Schenke, H.W.**, **Akhmetzhanov, A.M.**, **Satur, N.**, **Zaragosi, S.**, **McDonnell, A.**, **Schenke, H.W.**, **Akhmetzhanov, A.M.**, **Satur, N.** and **Zaragosi, S.** (2003) Canyon heads and channel architecture of the Gollum Channel, Porcupine Seabight. In: *European Margin Dynamics. Side-Scan Sonar and Seismic Images* (Eds Mienert, J. and Weaver, P.), pp. 183–186. Springer, Berlin.

Wheeler, A.J., **Kozachenko, M.**, **Beyer, A.**, **Foubert, A.**, **Huvenne, V.A.I.**, **Klages, M.**, **Masson, D.G.**, **Olu-Le Roy, K.** and **Thiede, J.** (2005) Sedimentary processes and carbonate mounds in the Belgica Mound province, Porcupine Seabight, NE Atlantic. In: *Cold-Water Corals and Ecosystems* (Eds Freiwald, A. and Roberts, J.M.), pp. 533–564. Springer, Berlin, Heidelberg.

White, M. (2007) Benthic dynamics at the carbonate mound regions of the Porcupine Sea Bight continental margin. *Int. J. Earth Sci.*, **96**, 1–9.

White, M. and **Dorschel, B.** (2010) The importance of the permanent thermocline to the cold water coral carbonate mound distribution in the NE Atlantic. *Earth Planet. Sci. Lett.*, **296**, 395–402.

White, M., **Roberts, J.M.** and **van Weering, T.** (2007) Do bottom-intensified diurnal tidal currents shape the alignment of carbonate mounds in the NE Atlantic? *Geo-Mar. Lett.*, **27**, 391–397.

Wienberg, C. and **Titschack, J.** (2015) Framework-forming scleractinian cold-water corals through space and time: a Late Quaternary North Atlantic perspective. In: *Marine Animal Forests* (Eds Rossi, S., Bramanti, L., Gori, A. and del Orejas Saco Valle, C.), pp. 1–34. Springer International Publishing, Cham, Switzerland.

Wienberg, C., **Titschack, J.**, **Frank, N.**, **De Pol-Holz, R.**, **Fietzke, J.**, **Eisele, M.**, **Kremer, A.** and **Hebbeln, D.** (2020) Deglacial upslope shift of NE Atlantic intermediate waters controlled slope erosion and cold-water coral mound formation (Porcupine Seabight, Irish margin). *Quataern. Sci. Rev.*, **237**, 106310.

Wils, K., **Wermersche, M.**, **Van Rooij, D.**, **Lastras, G.**, **Lamy, F.**, **Arz, H.W.**, **Siani, G.**, **Bertrand, S.** and **Van Daele, M.** (2021) Late Holocene current patterns in the northern Patagonian fjords recorded by sediment drifts in Aysén Fjord. *Mar. Geol.*, **441**, 106604.

Zomer, J.Y., **Naqshband, S.**, **Vermeulen, B.** and **Hoitink, A.J.F.** (2021) Rapidly migrating secondary bedforms can persist on the lee of slowly migrating primary river dunes. *Case Rep. Med.*, **126**, e2020JF005918.

Manuscript received 19 December 2024; revision accepted 20 December 2025

Supporting Information

Additional information may be found in the online version of this article:

Figure S1. Core B2306-GC02. From left to right: grain size distribution plots coloured according to the mode (with darker green representing a coarser mode) and mean grain size predicted from XRF data plotted in black; core photograph; CT scan; magnetic susceptibility; gamma-ray density; age-depth model; lightness; red-green chromaticity; yellow-blue chromaticity; XRF centre-log ratios of Rb, Ba, Zr, Si, Sr, Ti, K, Fe, and Ca.

Figure S2. Core B2306-GC04. From left to right: grain size distribution plots coloured according to the mode (with darker green representing a coarser mode) and mean grain size predicted from XRF data plotted in black; core photograph; CT scan; magnetic susceptibility; gamma-ray density; age-depth model; lightness; red-green chromaticity; yellow-blue chromaticity; XRF centre-log ratios of Rb, Ba, Zr, Si, Sr, Ti, K, Fe and Ca.

Supplementary Material S1. Details on Bayesian age-depth modeling for cores B2306-GC02 and B2306-GC04.

Supplementary Material S2. Detailed method for sediment core XRF scanning and high-resolution grain-size prediction.

Supplementary Material S3. Sequence of AUV photographs over megaripples in Bilbo Channel. For location, see Figure 5C.

Supplementary Material S4. Sequence of AUV photographs over cold-water corals in Bilbo Channel. For location, see Figure 7C.